

Modeling the Interaction Between Natural and Hydraulic Fractures Using 3D Finite-Element Analysis

Aditya Nikam, Obadare O. Awoleke, and Mohabbat Ahmadi, University of Alaska, Fairbanks

Summary

We built a 3D geomechanical model using commercially available finite-element-analysis (FEA) software to simulate a propagating hydraulic fracture (HF) and its interaction with a vertical natural fracture (NF) in a tight medium. These newly introduced elements have the ability to model the fluid continuity at an HF/NF intersection, the main area of concern.

We observed that, for a high-stress-contrast scenario, the NF cohesive elements showed less damage when compared with the low-stress-contrast case. Also, for the scenario of high stress contrast with principal horizontal stresses reversed, the HF intersected, activated, and opened the NF. Increasing the injection rate resulted in a longer and wider HF but did not significantly affect the NF-activated length. Injection-fluid viscosity displayed an inverse relationship with the HF length and a proportional relationship with the HF opening or width. We observed that a weak NF plane temporarily restricts the HF propagation. On the other hand, a tougher NF, or an NF with properties similar to its surroundings, does not show this type of restriction. The NF activated length was found at its maximum in the case of a weaker NF and at nearly zero in the case of a stronger NF and an NF that has strength similar to its surroundings.

In this study we present the results for a three-layered 3D geomechanical model with a single HF and NF orthogonally intersecting each other, using newly introduced cohesive elements for the first time in technical literature. We also conducted a detailed sensitivity analysis considering the effect of stress contrast, injection rate, injection-fluid viscosity, and NF properties on this HF/NF interaction. These results provide an idea of how the idealized resultant fracture geometry will change when several fracture/fracture treatment properties are varied.

Introduction

The issue of HF and NF interaction has been numerically examined using software packages at both the laboratory and field levels. Warpinski and Teufel (1987) experimentally found that the HF propagated through joints and formed a multistranded and nonplanar fracture network. The presence of a similar network was also observed in core samples from tight-sandstone reservoirs. Warpinski (1993) and Fisher et al. (2002) interpreted some of the Barnett Shale microseismic data and found that the HF propagation and orientation was affected by the already existing NFs. Lancaster et al. (1992) conducted a core study and found that the HF can propagate along an NF, resulting in propped NFs. There are laboratory experiments described by several researchers, and Gu et al. (2011) examined frictional interfaces at various angles and stress values and determined their impact on HF propagation, arrest, or diversion on approaching an NF.

Jeffrey et al. (2009), Chuprakov et al. (2011), and Weng et al. (2011) conducted simulations to investigate the critical factors that affect the development of complex fracture geometry. These factors included the NFs, interfacial friction, and the stress anisotropy. Dahi Taleghani and Olson (2014) examined, in two dimensions, the interaction of HF with cemented NFs and found three potential/possible propagation paths. In the first case, the HF propagated through the sealed NF; in the second case, it was arrested at the NF; and, in the last case, it branched out after intersecting the NF. He and Hutchinson (1989) further extended the work by suggesting different scenarios. They proposed that the HF could be double-branched or single-branched on the intersecting NF. Dahi Taleghani and Olson (2014) further studied the debonding and/or shearing of NFs during a hydraulic-fracturing process. The extended finite-element method was developed by Moës et al. (1999) and was applied by Lecampion (2009) to model HF along element edges. Lecampion (2009) did not address the fluid-flow coupling with HF propagation. Further fluid flow was coupled to this work to make the model more complex and realistic by Dahi Taleghani (2009). Dahi Taleghani and Olson (2014) showed that when an HF is parallel to the NF, a debonding/opening of the NF will occur ahead of the HF tip or side. Olson and Pollard (1991) reached similar conclusions. Offenberger et al. (2013) evaluated the Schlumberger Unconventional Fracture Model (UFMSM) module through HF/NF modeling coupled with reservoir simulation. Various UFM simulations were run and HF geometry was observed to be most sensitive to NF density and orientation. Sensitivity analyses were also performed to observe the impact of stress orientation, anisotropy, and shadowing on the distribution of the fracture network. However, this study did not consider interaction at the microlevel. Chuprakov et al. (2013) studied the propagation behavior of HF through NFs and accounted for the effects of fluid properties and NF permeability. Kresse and Weng (2013) further refined the UFM, taking into consideration the fluid leakoff into existing permeable NFs. According to them, the HF could propagate through the NF, open the NF, or be arrested at the intersection. Nolte and Smith (1981), Nolte (1991), Warpinski (1991), Barree and Mukherjee (1996), and Mukherjee et al. (1991) incorporated the observation that the presence of NFs alters the leak-off into the formation and that the permeability of NFs is both time and pressure dependent. Walsh (1981) investigated the effect of stress and pressure changes on NF permeability.

Aimene and Nairn (2014) modeled the propagation and interaction of multiple HF with NFs using the material point method. They considered an HF and an NF at different angles, with respect to maximum horizontal stress, and studied the effects of varying stress anisotropy and angle of NF on propagation for a Marcellus Shale gas well. Blanton (1982), Warpinski and Teufel (1987), and Sesetty and Ghassemi (2012) neglected the stress-shadowing effects in their analysis. Hence, mechanical interaction was not completely considered. However, numerical models developed by Koshelev and Ghassemi (2003) considered these interactions but did not consider the fluid flow. Zhang and Jeffrey (2006) included fluid flow and obtained results for a single NF. Weng et al. (2011) modeled HF with multiple

NFs and studied the effects of stress shadowing on propagation. [Fu et al. \(2011\)](#) simulated HF propagation in a randomly distributed NF network. [Sesetty and Ghassemi \(2012\)](#) developed a numerical model that coupled fluid flow with stress shadowing to simulate complex fracture networks and studied the evolving fracture geometry, fracture aperture, and pressures as a function of injection time to determine possible locations for proppant screenouts and secondary-fracture initiation.

[Nagel et al. \(2011\)](#) studied NF shear using continuum and a 2D discrete-element-method (DEM) code, varied matrix stiffness, and Poisson's ratio, and observed no changes in NF shear for constant mechanical properties of the NF. [Nagel et al. \(2012\)](#) developed a fully coupled discrete-fracture-network (DFN) model to study HF development in the presence of NFs. They considered the mechanical properties of NFs, such as elastic moduli, strength parameters, and fracture toughness. [Nagel et al. \(2012\)](#) studied the same NF shear with a 2D DEM code to consider matrix properties, DFN effects, and fracture friction angle, and observed that the friction angle had a greater effect on the NF shear. [Nagel et al. \(2012\)](#) also considered the pressure diffusion during hydraulic fracturing and found that the NF shear strongly depended on NF pressure that, in turn, ultimately depended on initial fracture aperture. [Oussoltsev et al. \(2013\)](#) developed a workflow to simulate HFs in Eagle Ford Shale using a reservoir-centric stimulation design tool. They presented the NFs as a 2D DFN with no limitation on vertical height with the ability to model proppant transfer. [Ben et al. \(2012\)](#) coupled the DEM and a discontinuous deformation analysis fluid pipe network model and simulated pressure response during hydraulic fracturing. [Gong et al. \(2011\)](#) studied a shale-gas reservoir to consider NFs by explicitly applying a DFN approach. They considered mechanisms such as gas adsorption/desorption, matrix/fracture transfer, and non-Darcy effects. They conducted a history match on the basis of 2 months of production data, and predicted cumulative gas production and gas rate for the next 3 years.

[Shin and Sharma \(2014\)](#) studied various HF design parameters that influence the resulting HF geometry and HF propagation patterns using FEA software. Simulations with different varying parameters were run, including perforation cluster spacing, number of perforation clusters, fracture height, fracturing-fluid viscosity, pumping rate, and Young's modulus. They considered multiple HFs in a target zone with surrounding layers and studied the resulting geometry with respect to job design parameters and some rock properties. [Yadav \(2011\)](#) developed a geomechanical model in FLAC® 2D software to study the HF/NF interaction by simulating the path followed by the HF once it intersects an NF. They also studied the extent of a microseismic-activity cloud when a naturally fractured medium was hydraulically fractured. In addition, they conducted a sensitivity analysis to observe the effect of different parameters on the extent of the microseismic cloud.

[Abbas et al. \(2014\)](#) modeled HFs to investigate the effect of fracture growth and reduction in a fracture opening at fracture offset for different combinations of parameters, such as formation moduli, far-field stresses, fluid-injection rate, and the ratio of offset length to the length of the straight fractures and the offset angles. The modeling was performed using a code based on the extended finite element method (XFEM). They pointed out that studying the interaction between HFs and weak planes could identify if the HF propagates through the weak planes, gets blunted and stops at the interface, or just propagates in the offset direction. Stress contrast, orientation angle, and interface friction were identified as some of the parameters affecting these interactions. [Abbas et al. \(2014\)](#) only discussed the geometry effects of these HF/NF intersection angles, when the difference between the vertical confining stress and the minimum principal horizontal stress was kept at zero. [Meng and De Pater \(2011\)](#) used COMSOL Multiphysics® to study the HF/NF interaction, observing the HF propagation once it intersects the NF. They developed a fracture-width profile—fluid pressure inside the fracture and leakoff rate along the length of the fracture.

[Fu et al. \(2015\)](#) studied the specific scenario of the HF propagating through the NF. They found the crossing phenomenon to be unique for the 3D case and realistic compared to the 2D analysis. They used a fully coupled hydraulic-fracturing simulation code, GEOSTM, and studied the HF/NF interaction with NFs perpendicular to the HF propagating direction. They conducted laboratory analysis and then simulated and studied a field-scale model. One of their key findings was that the HF always crossed the NF if the cementitious material filling the NF was very thin. However, their study was restricted to **perpendicular NFs** (with respect to the hydraulic propagation direction) and consisted of a single matrix material.

[Suarez-Rivera et al. \(2013\)](#) conducted experiments to study the interaction of propagating cracks with discontinuities or planes of weakness. They conducted experiments on outcrops of the Niobrara Formation. They measured the fracture conductivity for propped and unpropped cracks at varying stresses. They found that, with increasing stress, the conductivity of the fracture always remains higher for longer fractures than for shorter ones. They also mentioned that the distribution of proppant in the fractures is highly influenced by the complexity of the rock matrix or the discontinuities in the rock. They described the fracture system by **dividing it into four different segments: (1) the wellbore, (2) the connection between the wellbore and the fracture system, (3) near-wellbore fracture, and (4) far-field fracture.** Furthermore, they studied the consequences of each region on hydrocarbon production to determine the most prominent region for production decline. One aspect of their work was to observe the effect of weakness planes on crack propagation in laboratory samples. They studied and experimented with the effect of high, low, and no in-plane stress contrast on an induced fracture approaching weakness planes. These planes of weakness were at different orientations with respect to the direction of maximum horizontal stress. They defined a term called “step-over,” which is the shearing of an NF caused by the HF encountering it. This step-over is said to be always present in all of the scenarios considered; however, the step-over effect is clearest in the case of high-stress contrast and least apparent in the case of low-stress contrast. In the case of no-stress contrast, the HF was said to be arrested at the NF and followed the path of least resistance, which was supposed to be along the NF.

[Gonzalez-Chavez et al. \(2015\)](#) studied 2D HF/NF interaction using commercially available FEA software. They analyzed whether the HF was arrested by the NF, propagated through the NF, or followed the path of the NF upon intersecting the NF. The resulting geometry depends on the surrounding rock properties, magnitude and direction of principal horizontal stresses, and the angle between the intersecting fractures. They conducted a semicircular bending test to determine cohesive properties to be used in their FEA model. They examined four cases. The angle between the HF and NF was considered to be either 45 or 90°, with each orientation having either a weak or a strong NF leading to four different scenarios. In the case with a 45° intersection angle and weaker NF, the HF followed the path of the NF after intersection with activation of an NF wing. In the case with a 45° intersection angle and a stronger NF, the HF propagated across the NF without activating it. For the case with a 90° intersection angle and a weaker NF, the HF followed the path of the NF after intersection with activation of one of the NF wings. For the case with a 90° intersection angle and stronger NF, the HF propagated across NF without activating it. Furthermore, they considered a fifth case with four NFs perpendicular to the direction of maximum horizontal stress and four NFs parallel to the direction of maximum horizontal stress. In the case of the stronger NF, it was observed that the HF propagated through the NF and slightly sheared it—incomplete activation. In the case of the weaker NF, the HF approaching the NF was directed along the NF.

Recent work mostly considered a study and analysis of the HF/NF interaction, mainly in two dimensions. [Fu et al. \(2015\)](#) studied this interaction in three dimensions, mentioning the limitation or uncertainty in the 2D analysis for an HF propagating through an NF. Their study concluded that the results of an HF crossing an NF differ between three dimensions and two dimensions. In three

dimensions, the opening changes in relation to depth and, hence, the advancing HF tip profile propagating through the NF varies with depth. Their study considered a homogeneous single layer of rock and was performed using a GEOS code.

We observed from the literature review that the HF/NF interaction is being extensively studied with consideration of its importance in hydraulic-fracturing-job design. For this paper, we studied the HF/NF interaction in three dimensions using commercially available FEA software. This study is [the first \(to the best of the authors' knowledge\) to demonstrate use of the special-purpose advanced cohesive pore-pressure elements available in FEA software](#), which are capable of modeling fluid continuity at the HF/NF intersection in three dimensions. These advanced elements were used to define planes that specify or define the direction of the HF and represent the NF as a plane of discontinuity.

Model Construction

A commercially available FEA software was used for this study. A single HF was modeled with the target and surrounding formations in the presence of a single NF. The actual reservoir case was simplified to a rectangular cuboid geomechanical model, as shown in **Fig. 1**. A vertical HF propagation path was predefined, and a single vertical NF was modeled, as shown in **Figs. 1 and 2**. Potential drawbacks to using a predefined HF path [and assuming orthogonal HF/NF intersections are discussed in a later section of this work](#). The HF was represented by an orange plane and the NF by a green plane. The overburden stress was denoted as S_v , and the maximum and minimum horizontal stresses were denoted as S_{Hmax} and S_{Hmin} , respectively. In **Fig. 2**, the left figure shows the top view and the right figure shows the side view of the 3D geomechanical model.

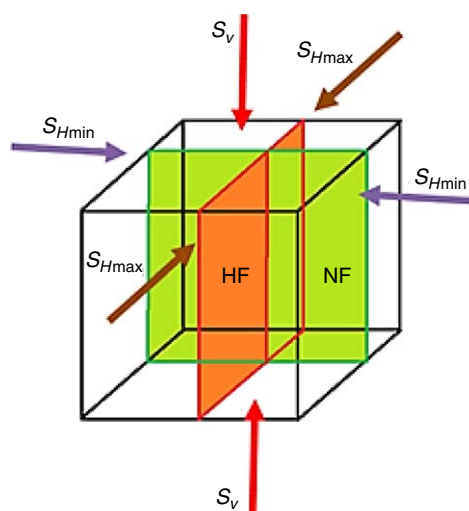


Fig. 1—3D geomechanical model representing a single HF in orange and a single NF in green.

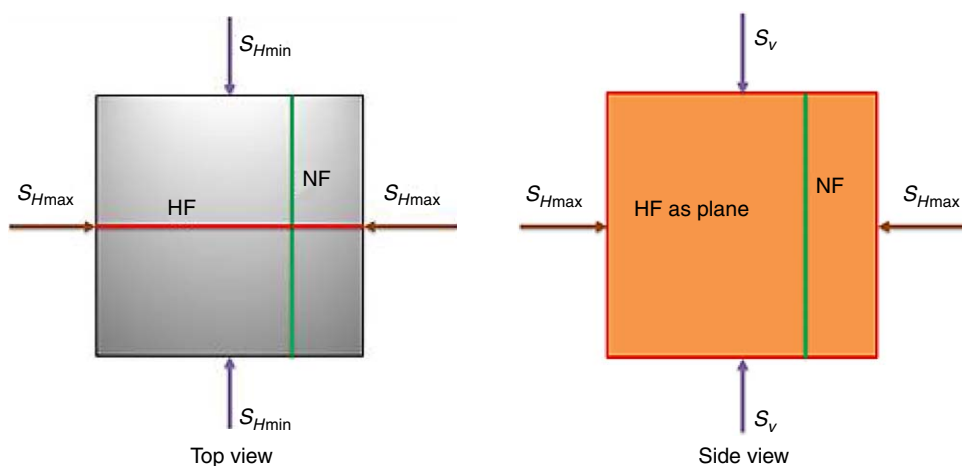


Fig. 2—2D planar top and side views of the 3D geomechanical model.

The NF and HF planes were constructed using 3D advanced cohesive pore-pressure elements—[COD3D8P](#). The rock matrix was considered a porous elastic medium and was modeled using reduced integration hexahedral pore-pressure and stress elements—C3D8RP. There were 12 and 8 nodes of each element type, COD3D8P and C3D8RP, respectively. The target layer was surrounded by top- and bottom-bounding layers to include the effect of the surrounding layers. The node defining the HF/NF intersection was kept common to allow fluid flow continuity in all directions. The meshed geomechanical model created using FEA software is shown in **Fig. 3**. The geomechanical model had dimensions of [250, 500, and 43 m](#) in the x -, y -, and z -directions, respectively, as shown in **Fig. 4**. The cohesive planes were imbedded in the rock matrix, as seen in **Fig. 4**, where the surrounding rock matrix was removed for proper visualization of the planes. The HF and NF were represented by a thin layer of cohesive planes. The HF dimensions were 250, 0.0015,

and 43 m in the x -, y -, and z -direction, respectively. Similarly, the NF had dimensions of 0.0015, 500, and 43 m in the x -, y -, and z -direction, respectively. For the base case, the total number of elements was 21,792 and total number of global nodes was 26,377. A finer mesh size was used closer to the fracture planes, and a coarser mesh size was used toward the model boundary. Mesh sensitivity analysis was conducted by varying the mesh sizes or number of elements in a 2D model. It was time-prohibitive to do this in a 3D model. The results indicated that the fracture-opening vs. fracture-length plot showed some sensitivity to the mesh size, but the results were convergent (Fig. 5). Because we considered relative effects and, given the amount of extra time the model required for the execution of the finer meshed models, proposed mesh sizes of 1×1 m closer to the fracture and 10×10 m at the model boundary was considered adequate. The cohesive elements along the edge of the target formation thickness were defined as open to permit liquid flow. Perforation frictional pressure drop and the effect of near-wellbore temperature transients on stress were not considered in this work.

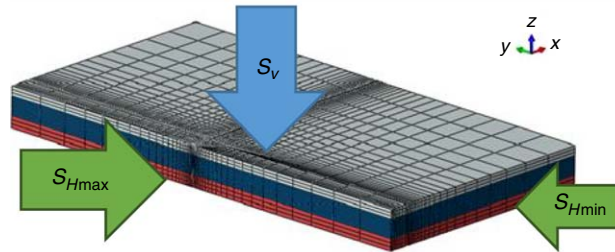


Fig. 3—Meshed 3D geomechanical model with target and surrounding layers. Distances in the x -, y -, and z -direction are 250, 500, and 43 m, respectively.

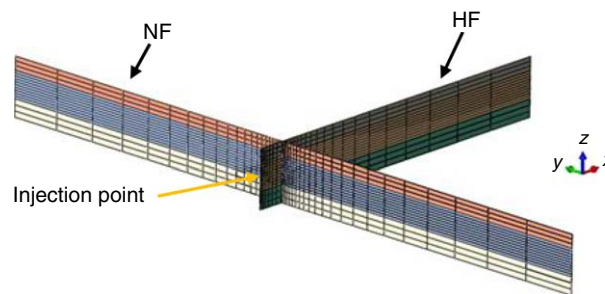


Fig. 4—HF and NF planes constructed using meshed cohesive element planes.

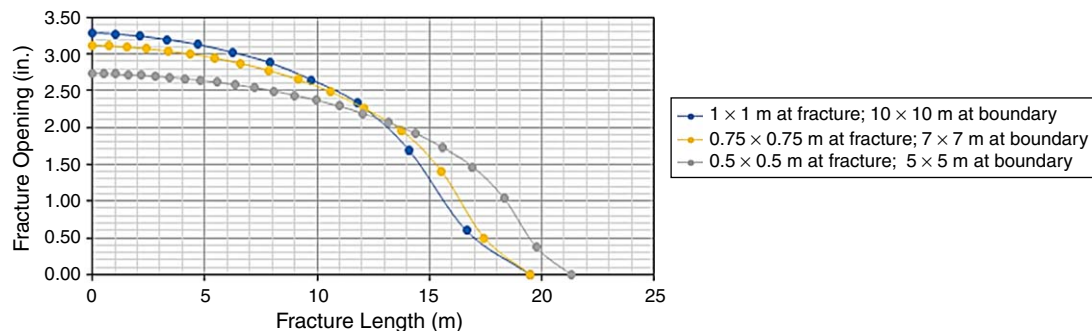


Fig. 5—Fracture opening for the sensitivity analysis.

There were two steps in the model: (1) A geostatic step, required to initialize the model with the initial stress/initial loading conditions and (2) a pump step, representing the actual fracturing process in which fracturing fluid was pumped for a certain period of time while the resulting fracture geometry was observed. The presence or effect of proppants in the fracturing fluid was not considered because the fracturing fluid actually creates the fracture and not the slurry. The injection rate was applied at the midpoint of the target formation at a single node and is denoted by a yellow arrow in Fig. 4. The black arrows in Fig. 4 show the HF and NF defining planes, with the NF plane being perpendicular to the defined injection direction or maximum horizontal stress.

The face of the model perpendicular to the injection load that contains the injection load is defined as the inner boundary, and the other three faces bounding the model are defined as the outer boundary. The remaining two faces are the top and bottom surfaces of the geomechanical model. The displacement and rotation in the x - and y -direction were fixed on the outer boundary and the inner boundary was modeled to be symmetric along the x -axis. The displacement and rotation of the model bottom were fixed in the z -direction. Lithostatic pressure was applied to the top of the model. Pore pressure was applied to the top and bottom boundaries for equilibrium and initialization. The gravity effects were also considered in the model. During initialization, the void ratio, stress, and pore pressures were varied with depth. The permeability changed as a function of a porosity/void ratio. The NF was set at a 5-m distance from the injection point for the base-case scenario, which will be discussed in detail later. The length of the model in the HF-propagation direction was 250 m, the model length perpendicular to the HF-propagation direction was 500 m, and the total thickness was 43 m.

Hydraulic fracturing, in general, involves the coupling of several physical processes: namely, **porous-media deformation, fluid flow in fractures, fluid leakoff into the formation, fluid flow in porous media, and fracture initiation and propagation**. Each of these processes has been thoroughly investigated in the literature, and good summaries can be found in the works of Shin and Sharma (2014), Zielonka et al. (2014), and Searles et al. (2016). For clarity, however, it is necessary to state here that the HF/NF initiation and propagation problem was handled using continuum-damage mechanics. The governing equations are summarized later.

Rock Deformation

The formation rock considered in this model was poroelastic and isotropic material that can undergo deformation. The constitutive equation governing the porous-rock deformation for small strains was defined using Eq. 1 (Zielonka et al. 2014):

$$\sigma'_{ij} - \sigma'^0_{ij} = 2G\varepsilon'_{ij} + \left(K - \frac{2}{3}G\right)\varepsilon'_{kk}\delta_{ij}, \quad \dots \dots \dots (1)$$

where $\sigma'_{ij} = \sigma'_{ij} + p\delta_{ij}$ is Terzaghi's effective stress and $\varepsilon'_{ij} = \varepsilon_{ij} - \frac{\alpha - 1}{3K}(p - p_0)\delta_{ij}$ is Terzaghi's effective strain. The variable α is Biot's constant, G is the shear modulus, K is the bulk modulus, and δ_{ij} is Kronecker's delta, which is defined as $\delta_{ij} = 1$ for $i = j$ and $\delta_{ij} = 0$ for $i \neq j$. Also, p is the pore pressure and p_0 is the initial pore pressure. The subscript 0 corresponds to the initial value, and the subscript kk corresponds to summation under Einstein's convention.

Modeling Fluid Flow

The fluid flow in this model can be characterized as (1) the fluid flow in the crack or the fracture, (2) the fluid leakoff from the fracture surfaces, and (3) the fluid flow in the porous media. The tangential flow in the fracture was modeled as the Poiseuille flow using Eqs. 2 and 3 (Shin and Sharma 2014):

$$q = -k_t \nabla p, \quad \dots \dots \dots (2)$$

$$k_t = \frac{d^3}{12\mu}, \quad \dots \dots \dots (3)$$

where k_t is the tangential permeability resistant to flow in the Poiseuille flow equation, ∇p is the pressure gradient along the cracked element surfaces, d is the cracked element opening, and μ is the viscosity of the fluid being injected.

The leakoff from the fracture surface to the formation was modeled as a normal flow through a permeable membrane, as described in Eqs. 4 and 5 (Shin and Sharma 2014):

$$v_t = c_t(p_i - p_t), \quad \dots \dots \dots (4)$$

$$v_b = c_b(p_i - p_b), \quad \dots \dots \dots (5)$$

where c_t and c_b are the top and bottom fluid-leakoff coefficients, respectively, kept equal in our study. The variables v_t and v_b are the flow velocities into the top and bottom surfaces of the cracked element. Also, p_i , p_b , and p_t are the pressure inside the fracture, pressure outside the bottom face of the fracture, and pressure outside the top face of the fracture, respectively.

The fluid flow in the fracture was governed by Reynold's lubrication theory and was defined by a continuity equation (Charlez 1997). Substituting the Poiseuille flow equation and leakoff equations into the continuity equation resulted in Eq. 6 (Zielonka et al. 2014):

$$\frac{\partial d}{\partial t} + c_t(p_i - p_t) + c_b(p_i - p_b) = \frac{\partial}{\partial l} \left(\frac{d^3}{12\mu} \nabla p \right), \quad \dots \dots \dots (6)$$

where $q = -\frac{d^3}{12\mu} \nabla p$, $\frac{\partial d}{\partial t}$ is the change in the fracture opening per change in time, and $\frac{\partial q}{\partial l}$ is the change in the fracturing-fluid rate per change in fracture length.

Fracture Initiation and Propagation

Damage modeling consists of two processes: (1) damage initiation and (2) damage evolution. In this study, the damage was modeled using the bilinear traction separation law. A quadratic nominal stress criterion was used for modeling the damage initiation. According to this criterion, damage will commence in the cohesive element when the addition of the squares of the ratios of the stresses in the element to the ultimate stress or damage-initiation stress or nominal stress equals unity, thus satisfying Eq. 7 (Haddad and Sepehmoori 2014),

$$f = \left(\frac{\langle t_n \rangle}{t_n^o} \right)^2 + \left(\frac{t_s}{t_s^o} \right)^2 + \left(\frac{t_t}{t_t^o} \right)^2, \quad \dots \dots \dots (7)$$

where t_n^o , t_s^o , and t_t^o are the damage-initiation stresses in normal, shear, and tangential directions, respectively. The variables t_n , t_s , and t_t are the stresses in the element in normal, shear, and tangential directions, respectively. The notation $\langle \rangle$ is called a Macaulay bracket and indicates that no compressive forces will initiate damage.

The damage-evolution law governs the rate at which the stiffness of the cohesive elements is degraded once the damage initiates. The damage factor D has an initial value of zero when the element is not damaged and has a value of unity when the element is completely damaged or a fracture is induced. The variables T_n , T_s , and T_t denote the normal, shear, and tangential stress components in Eqs. 8 through 10:

$$t_n = (1 - D)T_n, \quad T_n \geq 0 \quad \dots \dots \dots (8)$$

$$t_s = (1 - D)T_s, \quad \dots \dots \dots (9)$$

$$t_t = (1 - D)T_t, \quad \dots \dots \dots (10)$$

The mixed mode failure criterion, used for damage evolution, is defined using the Benzeggah-Kenane criterion, as defined in Eq. 11 (Benzeggah and Kennane 1996):

$$G_{\text{equic}} = G_{\text{IC}} + (G_{\text{IIC}} - G_{\text{IC}}) \left(\frac{G_{\text{II}} + G_{\text{III}}}{G_{\text{I}} + G_{\text{II}} + G_{\text{III}}} \right)^\eta, \quad \dots \dots \dots (11)$$

where G_{equic} is the equivalent fracture energy release rate and G_{IC} and G_{IIC} are the critical fracture energies in Mode I and Mode II, respectively. Note that η is the material parameter whose value is 2 for brittle solids and 3 for ductile solids. The critical fracture energy was calculated using Griffith and Irwin's equation [i.e., $G_{\text{IC}} = K_{\text{IC}}^2 \frac{(1 - \nu^2)}{E}$], where K_{IC} is the fracture toughness, ν is Poisson's ratio, E is the modulus of elasticity, and G_{IC} is the critical fracture energy. The critical fracture energy in Mode II can be defined in a similar manner. Also, G_{II} and G_{III} are the fracture energies used by the system during the damage process.

Model Workflow

The workflow of the fracturing process is shown in **Fig. 6**. Step 1 was to prepare a global 3D field model specifying the rock properties for the target and adjoining layers. The HF and NF paths were then predefined in the model, with NF as a weak discontinuity represented by a thin cohesive elements plane. Step 2 was to initialize the model by calculating the initial geostress and the porosity/permeability distribution with respect to the specified boundary conditions and loads. Step 3 was the actual fracturing-fluid-injection stage where the fracturing fluid (i.e., slickwater for the base case) was injected into the nodes along the target formation thickness with specified boundary conditions. Step 4 demonstrated the actual fracture initiation and propagation following the traction separation law. The applied injection load overcame the cohesive element's traction forces and tears, thus shearing or damaging the cohesive elements along the predefined fracture path. Step 5 involves the fracture pressure calculations from the final fluid-flow continuity equation derived from the Poiseuille flow equation and leakoff equation for the fluid flow in a fracture. Finally, Step 6 automatically generates the fracture-opening values through the output variable identifier in the FEA software. The identifier is a result of the nodal displacements of the deformed rock. The fracture-geometry description, including the fracture width, height, and length, was obtained directly through the stiffness-degradation and fracture-opening output variable identifiers in the FEA software.

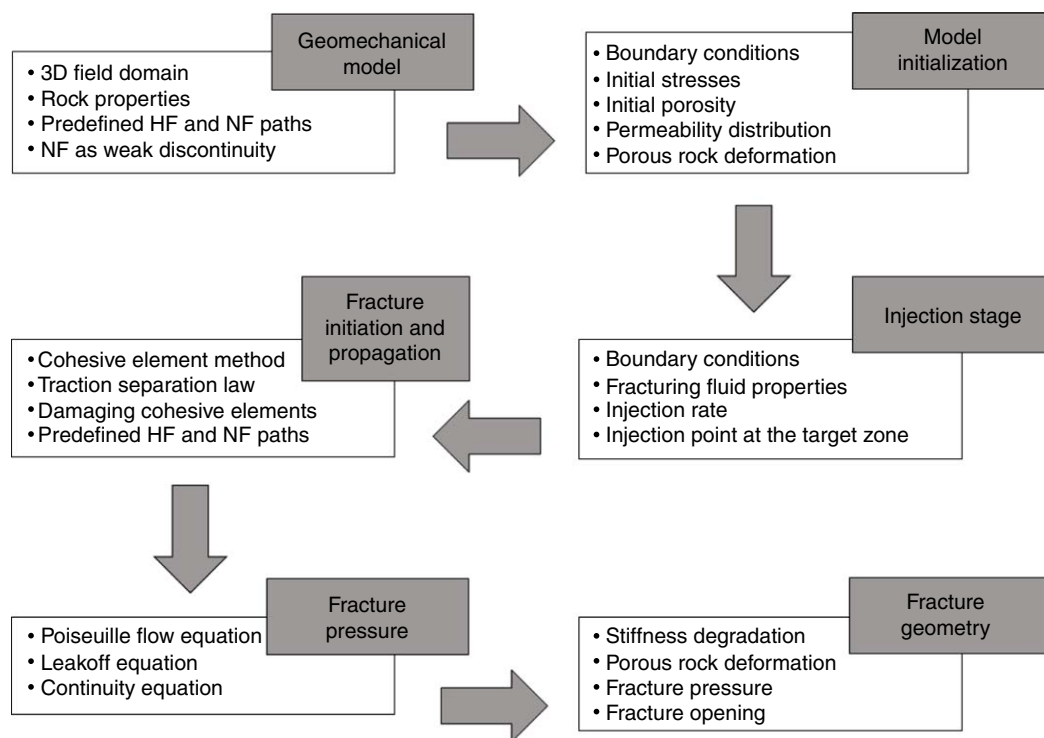


Fig. 6—Workflow of the fracturing process.

Model Validation

A geomechanical model with radial geometry and a single HF, found in the literature, was considered and reconstructed with a rectangular cuboid geometry. We were required to construct the model in such a cuboidal form to simplify the representation of HF and NF, as shown in Figs. 3 and 4. Pumping pressure over the injection time was obtained for the reconstructed model and was matched with the existing radial model, as shown **Fig. 7**. Here, the orange-colored data series represents **the pressure trend for the original radial geometry model from the literature**. On the other hand, the blue-colored data series represents **the pressure trend for our rectangular cuboid geometry model**. A similar type of validation methodology was used by Lu et al. (2015). The profile showed a satisfactory match, and the model was validated. The breakdown pressures (Fig. 7b) in our model showed less numerical instability (especially in

early time) than those in the validation model because we used a finer mesh in our work and because we used a cuboidal model as opposed to a radial one. Mesh sensitivity, in our case, was 1×1 m closer to the fracture and 10×10 m toward the model boundary, vs. 5×5 m closer to the fracture and 15×15 m toward the model boundary in the original data. Ideally, the model should be validated with the field data. However, because of the unavailability of field data, a general match with the radial model and stable/convergent output was considered sufficient for model validation.

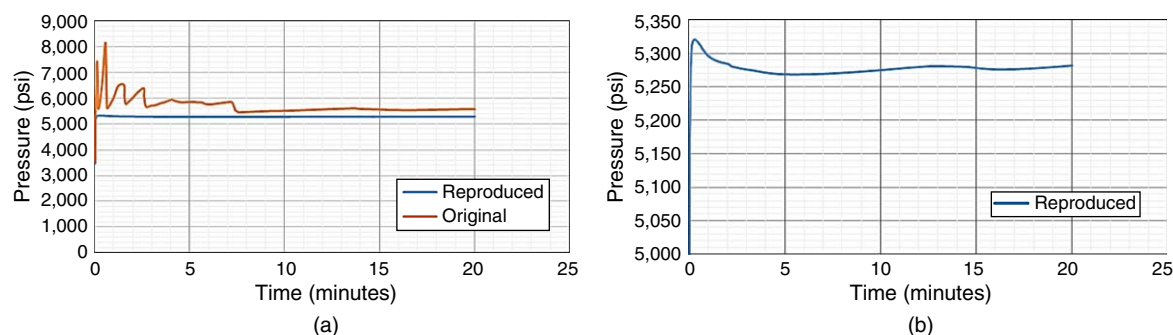


Fig. 7—(a) Fracture pressure curve for existing radial model and reconstructed model, (b) a closer look at the fracture pressure curve for the reconstructed pressure model showing pressure decline with less numerical instability.

Base Case

The base case was formulated using the guidelines provided by Gonzalez-Chavez et al. (2015). They considered scenarios with a weaker NF and a stronger NF in their 2D model. The NF was represented as a weaker and stronger discontinuity, respectively, with respect to the surroundings. Hence, the NF mechanical properties were represented by a factor times the mechanical properties of the HF or the surrounding medium (Gonzalez-Chavez et al. 2015). A factor of 0.3 was used for a weaker NF, with a factor of 1 corresponding to an NF similar to the surroundings and a factor of 3 corresponding to a stronger NF. Our main objective was to consider and study the HF/NF interaction, and, hence, the NF was considered to be weaker than the surrounding formation for the base case. An orthogonal HF/NF intersection was considered in this study. This type of intersection is found in Barnett Shale (Gonzalez-Chavez et al. 2015) and, hence, has practical significance. The existing model from the literature with a single HF had a low injection rate of approximately 15 bbl/min and a low injection-fluid viscosity or slickwater viscosity of 1 cp.

Also, the target formation Young's modulus was in the lower range of 1.74×10^6 psia. We decided to increase the base-case injection rate to 30 bbl/min, the injection-fluid viscosity to 50 cp, and the target formation Young's modulus to 3.00×10^6 psia, keeping in mind that the sensitivity-analysis range bracketed the base-case scenario. The predefined HF path was composed of a very thin layer (i.e., 0.0015 m) of special elements that deformed and were thereafter damaged on the basis of the applied fluid pressure. On the other hand, the elements defining the surrounding rock deformed but did not have the ability to damage. As such, we assigned material properties, including the modulus of elasticity, to the surrounding rock to calculate its deformation despite the presence of a predefined HF path. Also, in accordance with the work by Gonzalez-Chavez et al. (2015), in our base case, the NF was situated at a distance of 5 m from the injection point. The input data for the base case and for other sensitivity-analysis parameters is summarized in Table 1. The data set, including the minimum and maximum horizontal stress equations listed in Table 1, was from the FEA software user manual. Also, on the basis of a literature survey, a similar data set was used by Haddad and Sepehrmoori (2014), Shin and Sharma (2014), and Lu et al. (2015).

Note that the HF opening with HF height in this study is always at the wellbore, and the HF opening with HF length refers to a path along the center of the target zone or from injection point until the model boundary at 250 m. The HF opening (width) as a function of HF height in the presence of an NF, is shown for the base case in Fig. 8. As seen in Fig. 8, the HF opening profile with height was very uneven with maximum opening at top, medium at bottom, and least in the target zone. This was caused by the varying rock elastic properties—that is, the Young's modulus and Poisson's ratio—controlling the rock deformation/opening in the three zones, as expected on the basis of physics of the process. In Fig. 9, the HF opening decreased as a function of length, as expected. However, there was a dramatic drop in the opening after propagating through the NF at 5 m. This agreed with the laboratory findings of Suarez-Rivera et al. (2013). In their work, they mentioned that the propagating crack is always initially restricted by a weak discontinuity. This might be the reason for the initially higher HF opening as a function of the HF length. Once the HF propagates past the discontinuity, there is a sharp reduction in its opening. The NF did not open in the base-case scenario; however, the NF elements were damaged. In Fig. 10, the average opening pressure was observed to be $\approx 5,280$ psia with average values of $\approx 6,190$, $\approx 5,334$, and $\approx 5,014$ psia for vertical principal stress, maximum horizontal principal stress, and minimum horizontal principal stress, respectively. A small spike was observed closer toward the boundary of the model and, hence, was required to be studied, analyzed, and investigated. This was initially thought to be a boundary effect, but, for clarification, a larger model was constructed by increasing the dimension in the direction of HF propagation from 250 to 500 m. The results for the larger and smaller model matched, and, hence, the spike was considered as a numerical error or simulation noise and not a boundary effect (Figs. 11 through 13). As seen in Fig. 13, the HF lengths for both cases were the same (i.e., ≈ 150 m for the same injection rate of 30 bbl/min and injection time of 20 minutes, respectively). In Fig. 13, the additional values seen for the base-case longer data series (green) from ≈ 150 to 500 m was plotted to show the zero values for the HF opening.

The NF in the base case did not open; however, the NF was activated, evidenced from the intensity plots for stiffness degradation (SDEG) values for cohesive elements representing the NFs in Fig. 14. The elements having SDEG values between 0.9 and 1.0 were damaged, resulting in an induced fracture, as per the FEA software manual, Gonzalez-Chavez et al. (2015), Shin et al. (2014), and Haddad and Sepehrmoori (2014). The top and bottom cohesive plane elements were completely damaged. The target zone cohesive elements were not completely damaged, especially toward the model boundary (Fig. 14). This was because the top and bottom formations were mechanically weaker than the target formation. It was noted that the NF mechanical properties were based on the mechanical properties of the respective surrounding layers. The HF and NF openings are shown in Fig. 15. As mentioned previously, the NF was activated but not opened, while the HF opening is clearly seen in the fracture-opening plot in Fig. 15. Note, for all the intensity plots in three dimensions, the deformation was magnified by a factor of 200 for proper visualization of the deformation. The activated NF half-length in the top and bottom zones was 250 m (extended up to the model boundary) while in the target zone it was ≈ 150 m. The HF length as a function of depth and various layers is shown in Fig. 15.

Parameter	Top	Target	Low
Top depth (m)	2100	2110	2130
Bottom depth (m)	2110	2130	2143
Thickness (m)	10	20	13
S_v total (psia)	$0.89 \cdot \text{depth (ft)}$		
S_{Hmin} total (psia)	$0.75 \cdot S_{Hmax}$, $0.94 \cdot S_{Hmax}$ (default), $0.99 \cdot S_{Hmax}$		
S_{Hmax} total (psia)	$[0.72 \cdot \text{depth (ft)} - 399]$	$[0.72 \cdot \text{depth (ft)} - 254]$	$[0.72 \cdot \text{depth (ft)} - 327]$
Pore pressure (psia)	$0.51 \cdot \text{depth (ft)}$		
Initial porosity [fraction (average)]	0.22	0.27	0.30
Initial permeability [md (average)]	1.03	5.02	1.13
Poisson's ratio (fraction)	0.15	0.22	0.19
Young's modulus (psia)	6.01×10^5	3.00×10^6	9.07×10^5
Drucker-Prager friction angle (degrees)	30	36	28
Drucker-Prager dilation angle (degrees)	30	36	28
Formation density (psia/ft)	0.89		
Fracture toughness (psia-in. ^{1/2})	252	435	312
Damage initiation stress (psia)	14.5	45	14.5
Injection rate (bbl/min)	30		
Injection time (minutes)	20		
Injection-fluid density (kg/m ³)	1000		
Injection-fluid viscosity (cp)	50		
Leakoff coefficient (bbl/psia-min)	1.53×10^{-6}		

Table 1—Model input parameters for the base case and parameter ranges for all the other simulation runs.

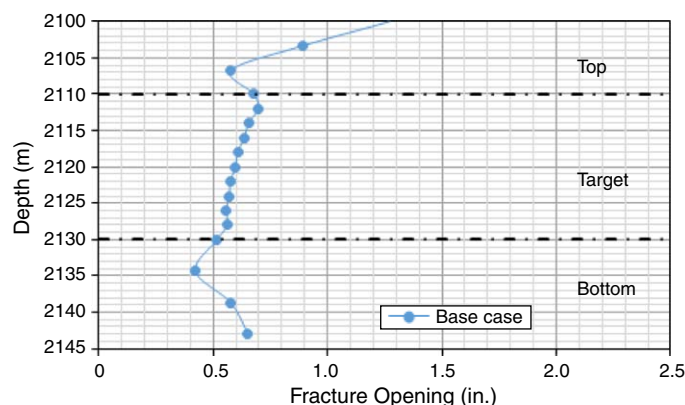


Fig. 8—HF opening as a function of HF height at the wellbore for the base case.

We used a lithostatic gradient of 0.89 psi/ft for the base case. Running the base case with a lithostatic gradient of 1 psi/ft did not result in a significant change in NF/HF behavior; therefore, we conducted the rest of the sensitivity analysis using a lithostatic gradient of 0.89 psi/ft.

Sensitivity Analysis

The hydraulic job design parameters and properties of the surrounding rock affected the behavior of the single- or multiple-propagating HFs. Some of the 2D FEA modeling performed by Lu et al. (2015) and Gonzalez-Chavez et al. (2015) also shed some light on the parameters that affected the interaction and geometry of an intersection of an HF and an NF. Apart from the simulation-based studies, laboratory analysis, such as that conducted by Suarez-Rivera et al. (2013), also mentioned the influence of some of the parameters on the HF and NF geometry or interaction. Hence, we presented a detailed sensitivity study on some of these important parameters with our more realistic and sophisticated 3D geomechanical model built using FEA to observe their effect on the resulting HF/NF geometry and interaction.

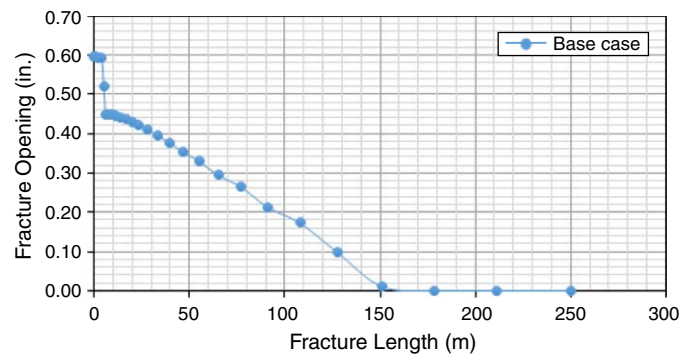


Fig. 9—HF opening as a function of HF length for the base case.

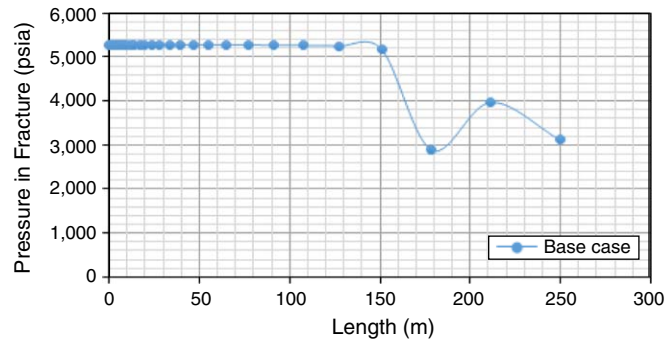


Fig. 10—HF pressure as a function of HF length for the base case.

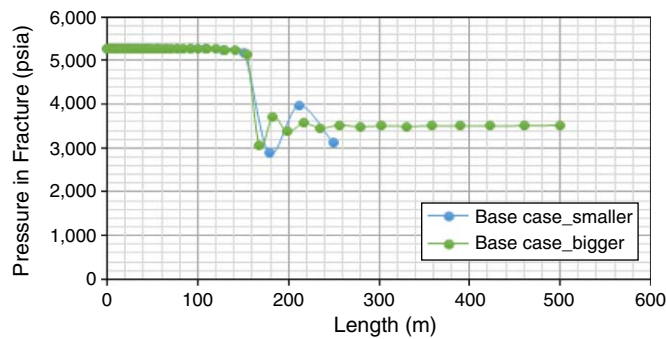


Fig. 11—HF pressure for dimensionally smaller and larger base-case model.

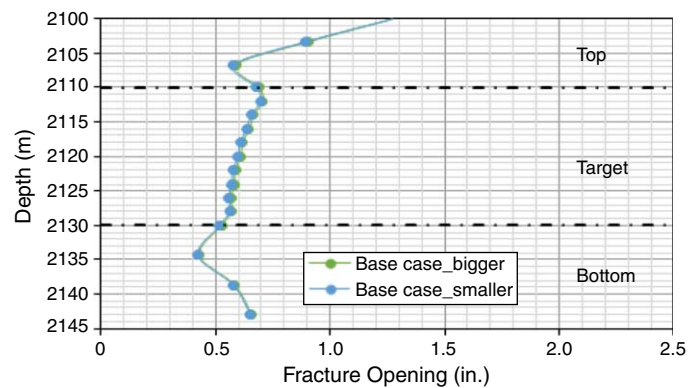


Fig. 12—HF opening for dimensionally smaller and larger base-case model.

The sensitivity analysis in this paper mainly considered the effect of job-design parameters, such as injection-fluid rate, injection-fluid viscosity, and some of the NF properties along with stress-contrasting effects, on the resulting HF/NF interaction and geometry. The various cases considered are summarized in **Table 2**.

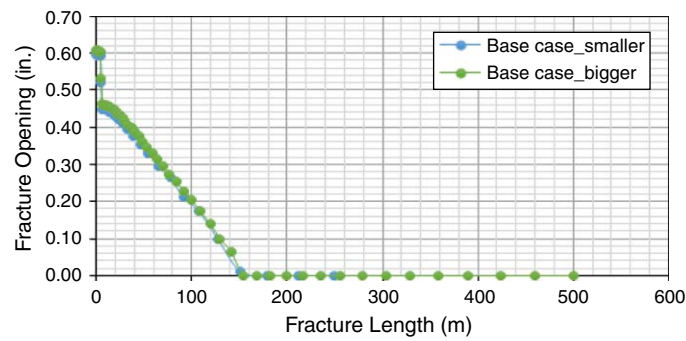


Fig. 13—HF opening for dimensionally smaller and larger base-case model.

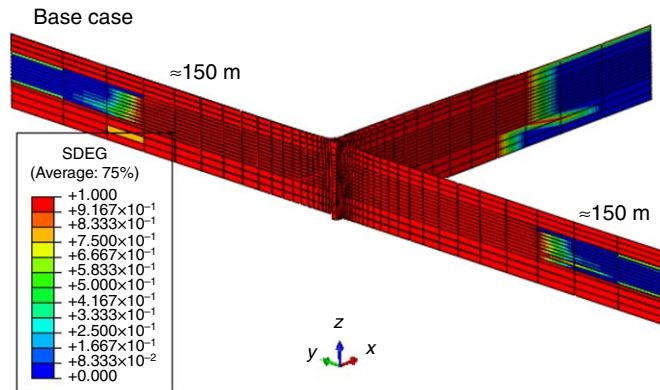


Fig. 14—SDEG plot for intersecting HF and NF planes at the end of pumping time for the base case.

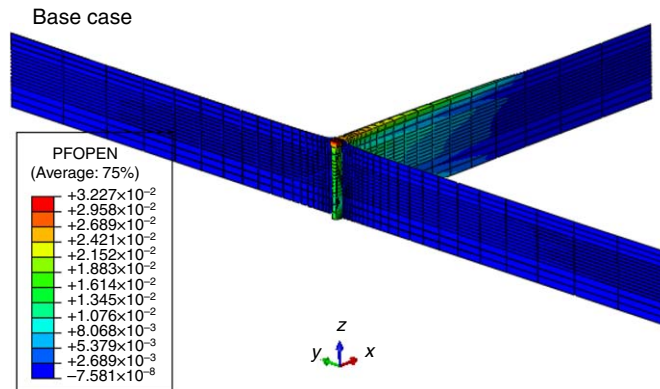


Fig. 15—Fracture opening for HF and NF planes at the end of pumping time for base case. PFOPEN = fracture opening output.

Case	Parameter	Explanation
1	$S_{Hmin} = 0.75 \cdot S_{Hmax}$	High-stress contrast (base case: $S_{Hmin} = 0.94 \cdot S_{Hmax}$)
2	$S_{Hmin} = 0.99 \cdot S_{Hmax}$	No-stress contrast (base case: $S_{Hmin} = 0.94 \cdot S_{Hmax}$)
3	Reversed S_{Hmin} and S_{Hmax}	High-stress contrast and stresses reversed
4	Injection rate = 15 bbl/min	Half of the base case of 30 bbl/min
5	Injection rate = 60 bbl/min	Twice the base case of 30 bbl/min
6	Injection-fluid viscosity = 10 cp	Lower than the base case of 50 cp
7	Injection-fluid viscosity = 1 cp	Slickwater
8	Injection-fluid viscosity = 100 cp	Higher than the base case of 100 cp
9	NF the same as the surroundings	NF strength the same as the surrounding rock (base case weaker NF, NF strength 0.3 times that of the surrounding rock)
10	Stronger NF	NF strength 3 times that of the surrounding rock (base case weaker NF, NF strength 0.3 times that of the surrounding rock)

Table 2—Different cases considered for sensitivity analysis.

Effect of In-Plane Stress Contrast. Suarez-Rivera et al. (2013) discussed the effect of in-plane stress contrast—the maximum- and minimum-horizontal stress contrast on the HF-approaching discontinuities in laboratory samples. On the basis of their work, we simulated similar stress-contrast scenarios in our model and compared the nature of our results to their experiment findings. The following four scenarios were considered and studied: (1) Base case—the stress contrast was low [i.e., minimum horizontal stress (S_{Hmin}) was 0.94 times the maximum horizontal stress (S_{Hmax})], (2) Case 1—the stress contrast was high (i.e., $S_{Hmin} = 0.75 \cdot S_{Hmax}$), (3) Case 2—the stresses were almost equal (i.e., $S_{Hmin} = 0.99 \cdot S_{Hmax}$), and (4) Case 3 with reversed S_{Hmin} and S_{Hmax} —here, the stress contrast was as high as Case 1, but the principal horizontal stresses were reversed.

The activated-NF lengths in the base case, Case 1, and Case 2 were similar at approximately 150 m (compare Figs. 14 and 16). However, in Case 1 (the highest stress contrast and no stress reversal), the target zone cohesive elements showed the least amount of damage. Furthermore, for the base case and Cases 1 and 2, the HF opened and propagated through the NF, as observed in Figs. 14 and 17. These results showed the same behavior or nature as seen in the laboratory results obtained by Suarez-Rivera et al. (2013), which found that, for high-stress-contrast scenarios, the propagating crack shears the weaker discontinuity and propagates through the discontinuity. Also, for the base case and Cases 1 and 2, the resulting HF geometry was similar (Figs. 18 through 21).

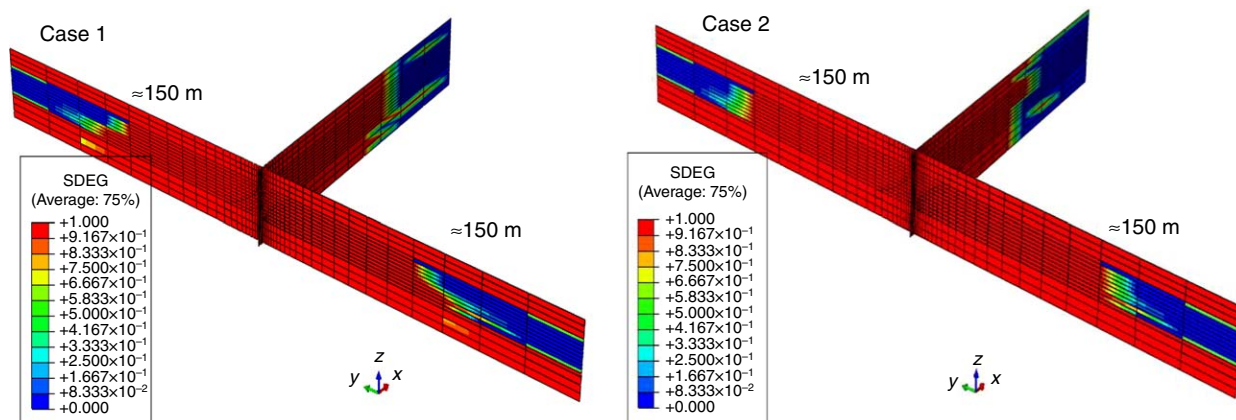


Fig. 16—SDEG plot for intersecting HF and NF planes at the end of pumping time for Case 1 ($S_{Hmin} = 0.75 \cdot S_{Hmax}$) and Case 2 ($S_{Hmin} = 0.99 \cdot S_{Hmax}$).

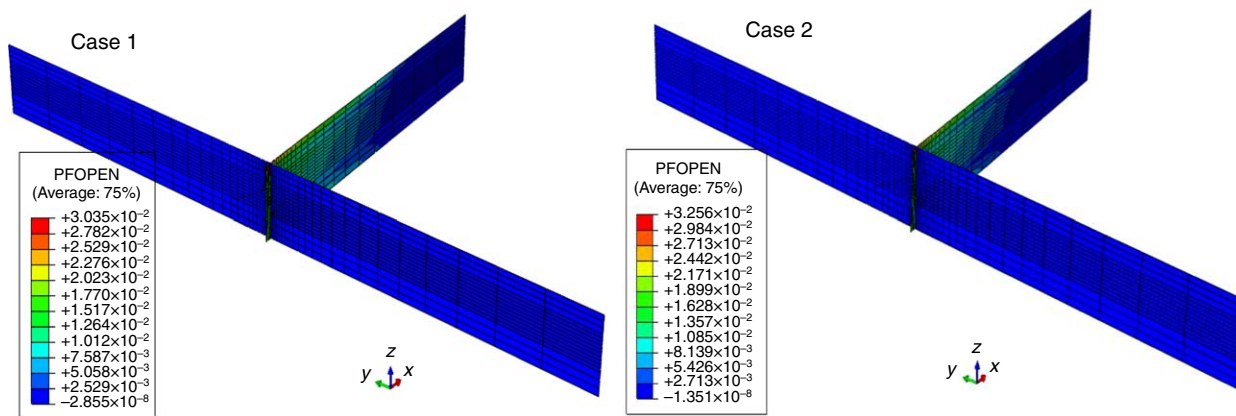


Fig. 17—Fracture opening for HF and NF planes at the end of pumping time for Case 1 ($S_{Hmin} = 0.75 \cdot S_{Hmax}$) and Case 2 ($S_{Hmin} = 0.99 \cdot S_{Hmax}$). PFOPEN = fracture opening output.

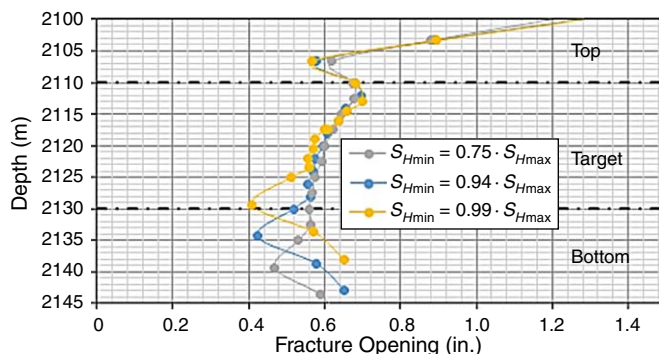


Fig. 18—Effect of stress contrast on HF opening at the wellbore.

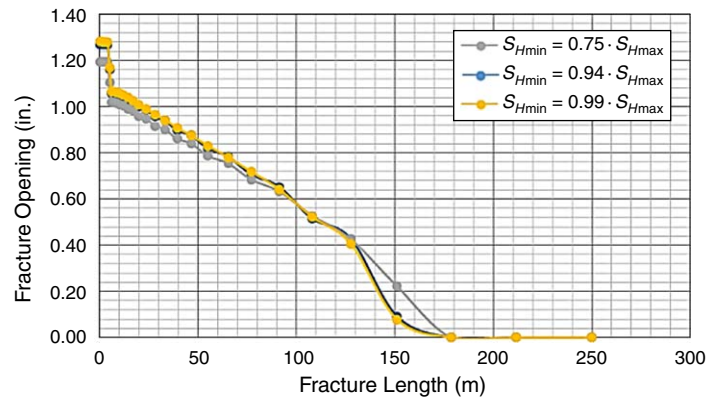


Fig. 19—Effect of stress contrast on HF opening as a function of HF length.

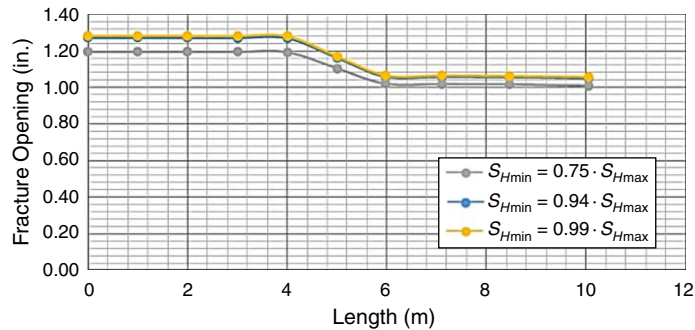


Fig. 20—Effect of stress contrast on HF opening while crossing NF.

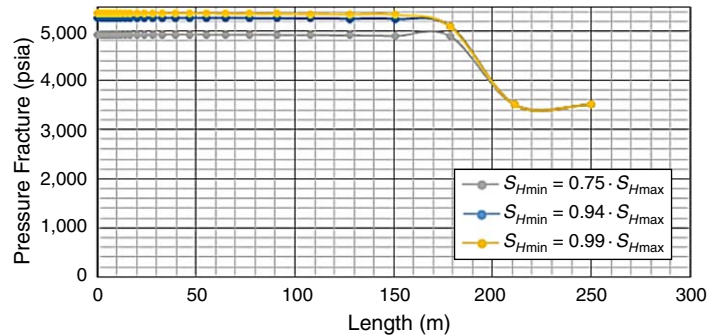


Fig. 21—Effect of stress contrast on HF pressure as a function of HF length.

For Case 3, as previously stated, the stress contrast was high, as seen in Case 1, but the stress directions were reversed. This was done to compare the laboratory observations of Suarez-Rivera et al. (2013) with a similar scenario. Both HF and NF opened for this scenario, and the HF was diverted into the NF, as seen in Fig. 22. Note, to reduce the computational time, the injection/simulation time was reduced from 1,200 seconds to 250 seconds. The injection rate was kept constant at 30 bbl/min. Also, the comparison used for Case 3 was the output from Case 1 at a total injection time of 250 seconds with a 30-bbl/min injection rate. Therefore, the results in Figs. 22 through 27 were at a constant injection rate of 30 bbl/min for 250 seconds. This was because the simulation for Case 3, under these conditions, took approximately 2 days on a desktop computer. However, no convergence issues or errors were observed. Fig. 23 shows the SDEG plot and that the NF was completely activated. This case should ideally result in an HF fracture with no intersection between the HF and the NF; however, because we predefined the HF plane, the HF barely opened, as seen in Figs. 22, 24, and 26 (yellow data series), but provided a path for the injection fluid. On applying the fluid pressure, the HF plane behaved like a sheared discontinuity diverting the fracturing fluid into the NF, thereby opening and extending the NF, as seen in Fig. 27. This observation was in general agreement with the laboratory findings of Suarez-Rivera et al. (2013).

Fig. 24 compared the HF opening with height for Case 1 (no stress reversal) and Case 3 (with stress reversal) after 250 seconds of injection time. The HF opening in Case 3 was smaller because of the activated and opened NF. Fig. 25 shows the NF opening at the HF/NF intersection with NF height. The NF did not open in Case 1 but did open in Case 3. Fig. 26 shows the HF opening as a function of HF length for both the cases. It was observed that the energy required to open the HF was being used to open the NF for a reverse-stress scenario. This resulted in virtually no HF openings for the reverse-stress scenario. Fig. 27 shows the NF opening as a function of NF length. The opened NF length was approximately 42 m. These observations supported the assertion that, in the reverse-stress scenario (Case 3), the HF growth was stunted as a result of NF growth.

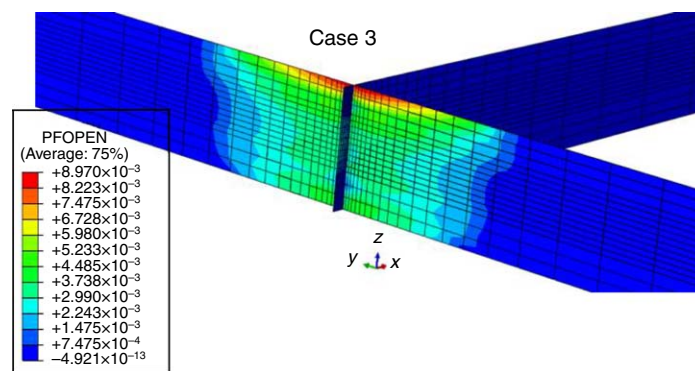


Fig. 22—Fracture opening for HF and NF planes at the end of pumping time for Case 3 (Case 1 with the stresses reversed). PFOPEN = fracture opening output.

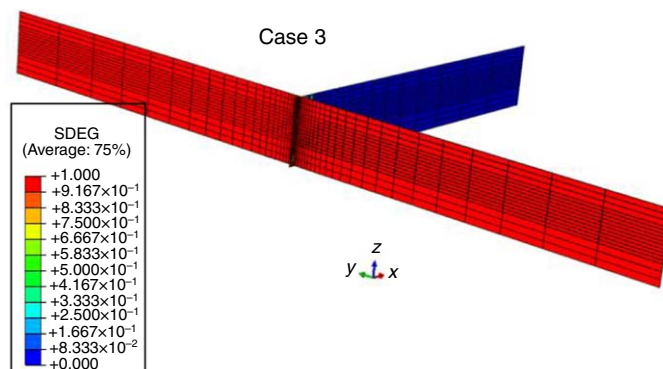


Fig. 23—SDEG plot for intersecting HF and NF planes at the end of pumping time for Case 3 (Case 1 with the stresses reversed).

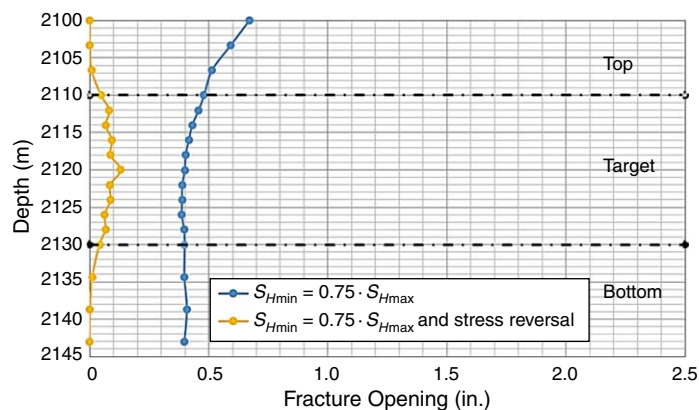


Fig. 24—Effect of stress reversal on HF opening at the wellbore after 250 seconds of injection.

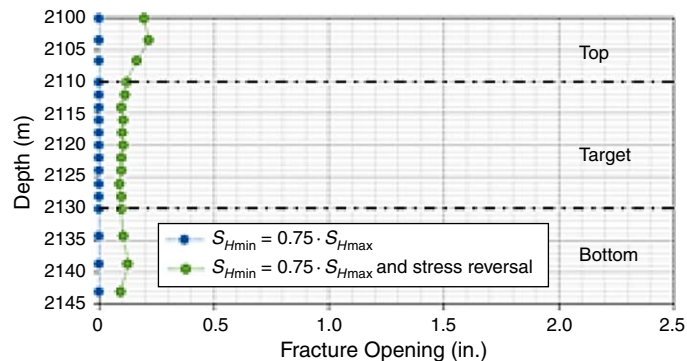


Fig. 25—Effect of stress reversal on NF opening at the HF/NF intersection after 250 seconds of injection.

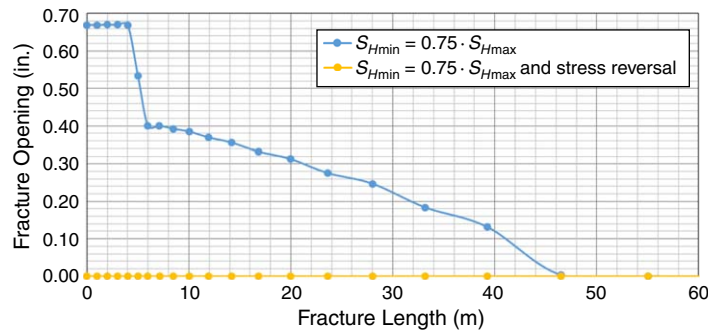


Fig. 26—Effect of stress reversal on HF opening as a function of HF length after 250 seconds of injection.

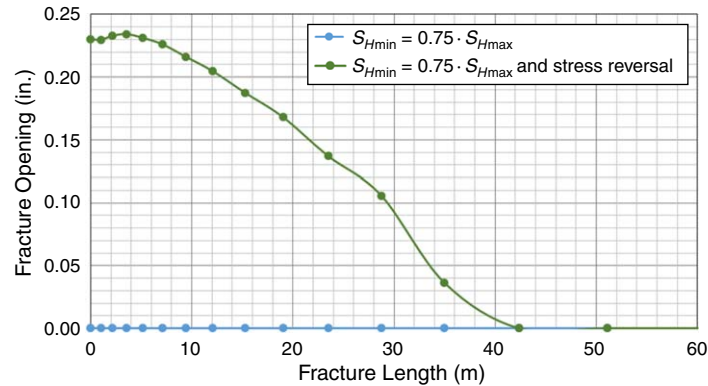


Fig. 27—Effect of stress reversal on NF opening as a function of NF length after 250 seconds of injection.

Effect of Injection Rate. The HF opening with height in the presence of an NF for different injection rates is shown in Fig. 28. As expected, the relationship between the HF opening and injection rate was proportional. Fig. 29 shows an HF opening as a function of HF length in the presence of an NF. There was a sudden drop in the HF opening after it propagated through the NF, as observed in previous cases. Fig. 30 gives a closer view of the HF opening while it propagated through the NF 5 m away from the injection point. The NF was activated for all three cases considered (compare Figs. 14 and 31). The NF in the top and the bottom layers was activated throughout to the model boundary for all three cases. Compared to the base case, changing the injection rate affected the HF geometry, but did not affect the NF geometry or activation profile. Fig. 32 shows the HF and NF openings in three dimensions with the activated NF remaining closed for all the injection-rate scenarios.

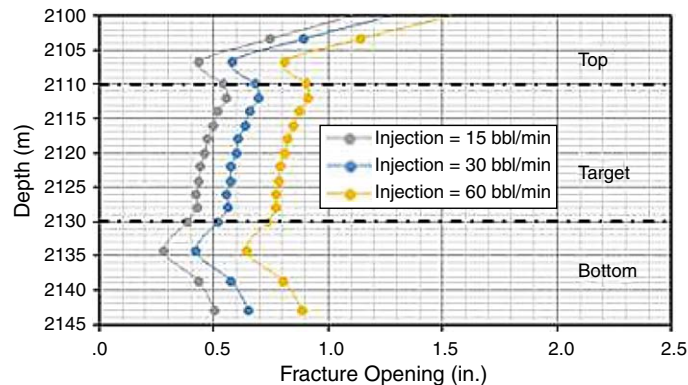


Fig. 28—Effect of injection rate on HF opening at the wellbore.

Effect of Injection-Fluid Viscosity. Fig. 33 shows a profile of an HF opening as a function of HF height in the presence of an NF with varying fluid viscosities. We can see that the HF opening increased as a function of increasing viscosity. In Fig. 34, the HF opening with HF length in the presence of an NF also shows an increase with increasing viscosity. However, the fracture length decreased with increasing viscosity. Fig. 35 gives a closer look at the HF opening at the HF/NF intersection (distance of 5 m from the injection point). A sudden drop in the HF opening was seen again after the HF propagated through the NF. However, the slope of the HF opening dropped as the HF/NF intersection changed and it seemed to flatten as the viscosity decreased (probably indicative of the proportional relationship between pressure drop; hence, fracture opening and viscosity). It can also be observed from Fig. 14 (base case) and Fig. 36 that the NF-activated length in the target zone decreased with decreasing viscosity and was observed to be the least in the case of slick-water (lowest viscosity). It should be noted that the activated NF length in the target zone was shorter when the contrast between the HF opening before and after the HF/NF intersection was smaller. Therefore, fracturing-fluid viscosity had an inverse relationship with

the HF length but a proportional relationship with the NF-activated length. The higher the viscosity, the larger the pressure drop at the intersection, leading to longer activated NF lengths for the high-end viscosity cases. To support the above reasoning, it was observed that the NF-activated length of ≈ 150 m for the base case (50 cp) changed to ≈ 180 m for Case 8 (100 cp) and to ≈ 105 m for slickwater (1 cp). **Fig. 37** shows the HF opening for Case 6 (10 cp) and Case 8 (100 cp). **Fig. 38** shows the SDEG plot for Case 7 (slickwater), and **Fig. 39** shows the HF opening in the presence of NF in three dimensions. The NF was activated but did not open.

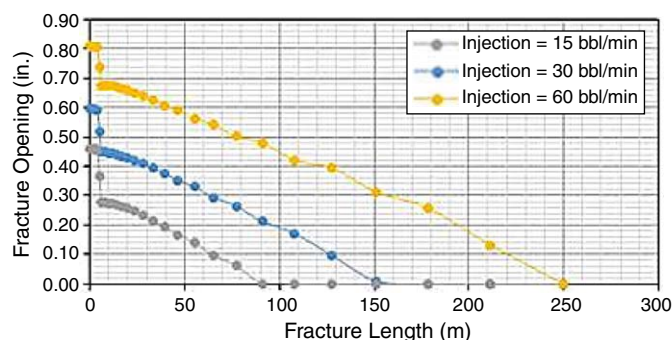


Fig. 29—Effect of injection rate on HF opening as a function of HF length.

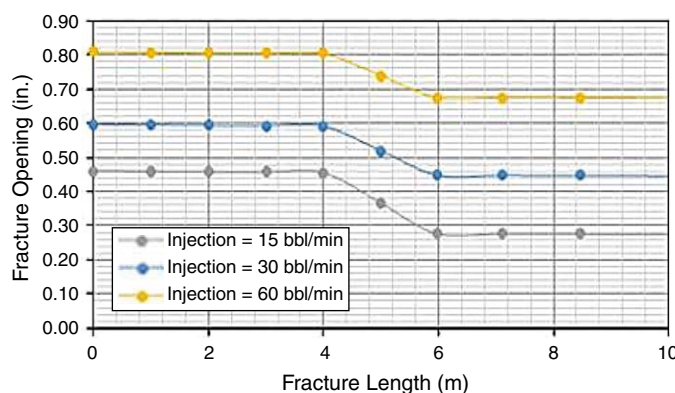


Fig. 30—Effect of injection rate on HF opening while crossing NF.

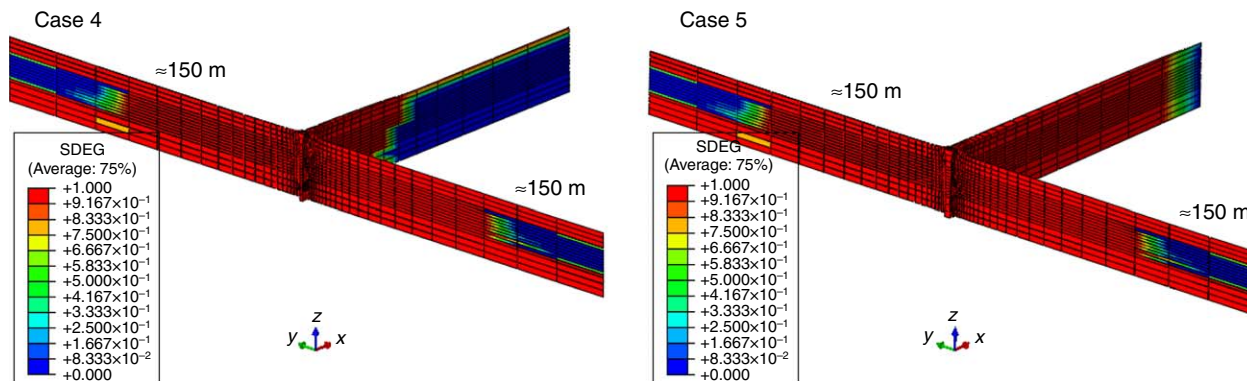


Fig. 31—SDEG plot for intersecting HF and NF planes at the end of pumping time for Case 4 (injection rate = 15 bbl/min) and Case 5 (injection rate = 60 bbl/min).

Effect of NF Strength. The fracture toughness and the damage-initiation stress were the main parameters multiplied by a factor to represent a weaker or stronger NF. The 2D studies conducted by Gonzalez-Chavez et al. (2015) led us to use a multiplier in this manner. In Suarez-Rivera et al. (2013), the laboratory experiments showed that the discontinuities or weakness planes encountered by propagating cracks temporarily restricted the propagating induced crack. **Fig. 40** shows that the opening of an HF encountering a weaker NF is larger compared with those with stronger discontinuities. This is probably because of the restriction created by the weaker discontinuity. The other two cases in which the NF was stronger or had properties similar to the surroundings were not seen as planes of weakness. Hence, the increase in the HF opening was not seen in these cases (**Figs. 41 and 42**). The HF plane was preset to open in the direction parallel to the NF orientation. The HF opening was reduced (**Figs. 40 and 41**) because additional energy had to be expended to overcome the additional toughness of the NF. For the stronger NF, the injection time (20 minutes), injection rate (30 bbl/min), and the surrounding rock properties were the same as for the base case. Therefore, compared with the base case, for the same injection volume, the HF tended to be longer (**Fig. 41**) because of the reduced HF opening in the stronger-NF case.

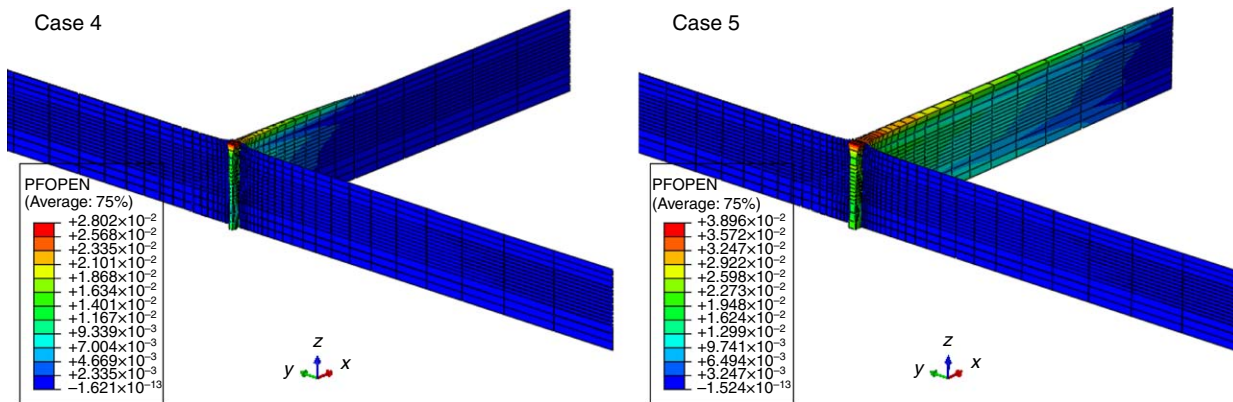


Fig. 32—Fracture opening for HF and NF planes at the end of pumping time for Case 4 (injection rate = 15 bbl/min) and Case 5 (injection rate = 60 bbl/min). PFOPEN = fracture opening output.

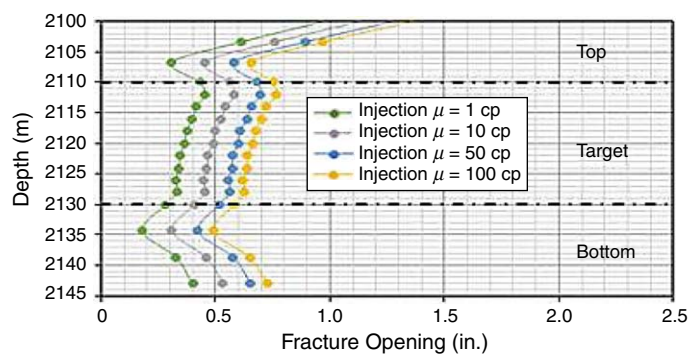


Fig. 33—Effect of injection-fluid viscosity on HF opening at the wellbore.

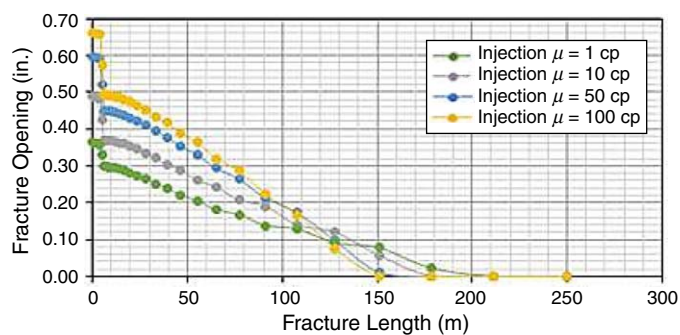


Fig. 34—Effect of injection-fluid viscosity on HF opening as a function of HF length.

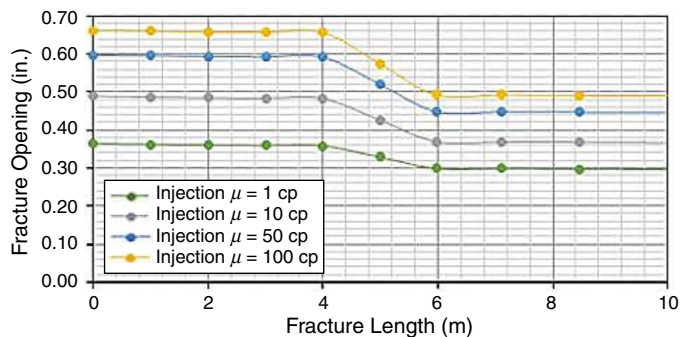


Fig. 35—Effect of injection-fluid viscosity on HF opening while crossing NF.

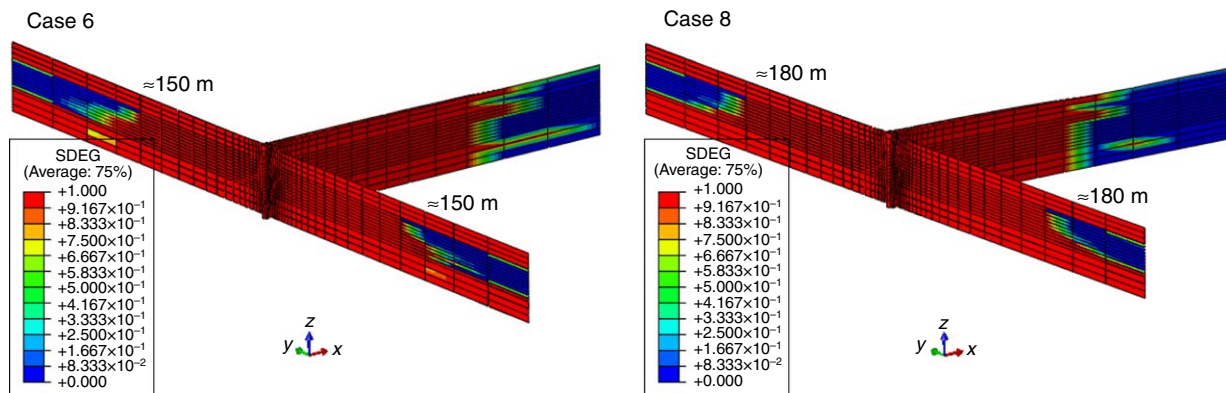


Fig. 36—SDEG plot for intersecting HF and NF planes at the end of pumping time for Case 6 ($\mu = 10$ cp) and Case 8 ($\mu = 100$ cp).

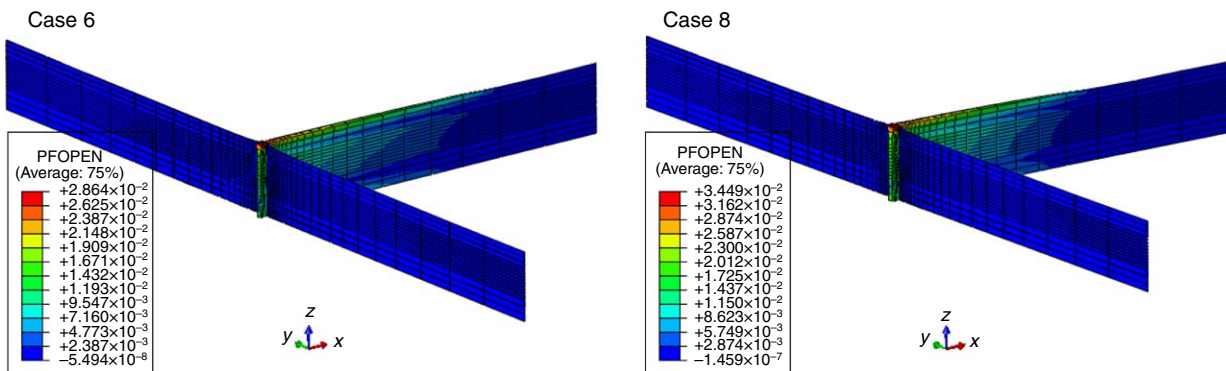


Fig. 37—Fracture opening for HF and NF planes at the end of pumping time for Case 6 ($\mu = 10$ cp) and Case 8 ($\mu = 100$ cp). PFOPEN = fracture opening output.

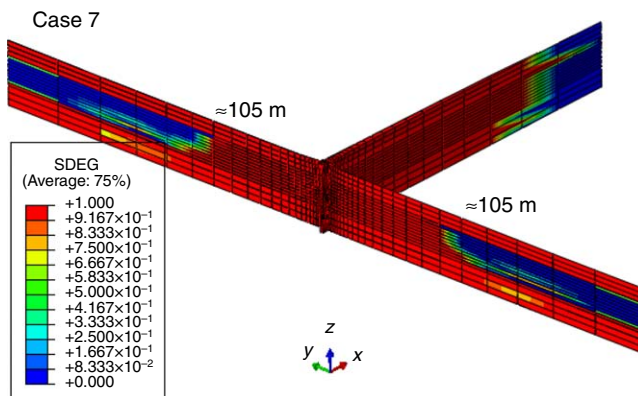


Fig. 38—SDEG plot for intersecting HF and NF planes at the end of pumping time for Case 7 ($\mu = 1$ cp).

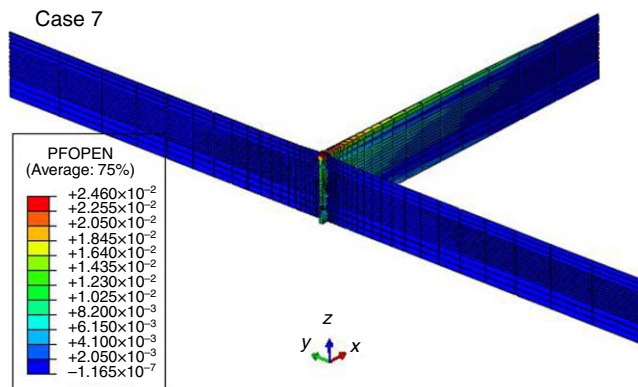


Fig. 39—Fracture opening for HF and NF planes at the end of pumping time for Case 7 ($\mu = 1$ cp). PFOPEN = fracture opening output.

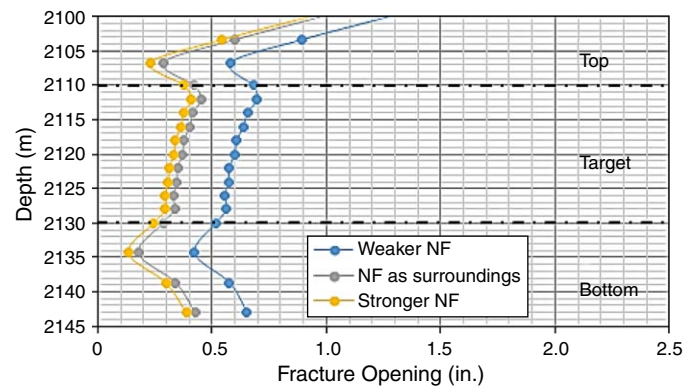


Fig. 40—Effect of NF strength on HF opening at the wellbore.

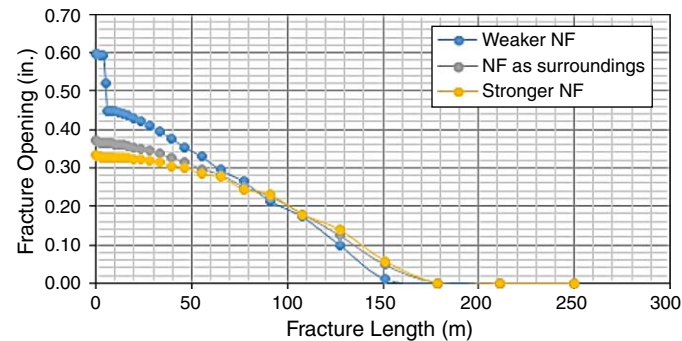


Fig. 41—Effect of NF strength on HF opening as a function of HF length.

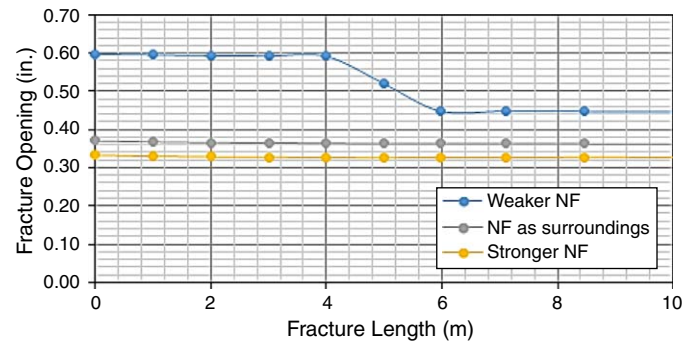


Fig. 42—Effect of NF strength on HF opening while crossing NF.

In Figs. 41 and 42, the HF opening in the presence of a weaker NF was large until it encountered an NF at 5 m. Thereafter, there was a rapid drop in the HF opening and then the opening profile followed the normal HF-propagation path. On the other hand, for the stronger NF and for the NF having properties similar to the surroundings, the HF opening as a function of HF length did not show a sudden drop. The discontinuity it encountered was not a weak plane, but rather a stronger one or one similar to the surroundings. The SDEG plots in Fig. 14 (base case, NF is weaker than the surrounding formation) and Fig. 43 clearly show that the NF was activated in the case of weaker NF and for an NF similar to the surroundings. The NF was not activated for Case 10 when the NF was stronger than the surrounding formation. Furthermore, Figs. 14 and 44 show the 3D view of an opened HF for weaker-NF and stronger-NF cases, respectively.

The observations for all the cases considered are summarized in Table 3.

Limitations of Work

In nature, NFs can exist as a cloud of cracks. However, in this study, we considered an idealized scenario in which we had an HF bisecting an NF orthogonally. Also, we used a predefined HF/NF path. This essentially means that the principal stress directions needed to be changed every time the HF path was redefined and vice versa, thereby limiting the model flexibility. Simultaneously propagating multiple HF's can also cause stress-shadowing effects that might affect the HF direction (Haddad and Sepehrnoori 2015).

Nonetheless, the results we described in this paper can help us characterize HF and NF behavior as a function of rock properties, stress magnitude, and direction- and job-design variables. We noted that experimentalists similarly idealized HF/NF propagation problems because of their complexity. Furthermore, it was reasonable to assume an orthogonal intersection between the HF and NF, as seen in the work of Gonzalez-Chavez et al. (2015) for the Barnett Shale.

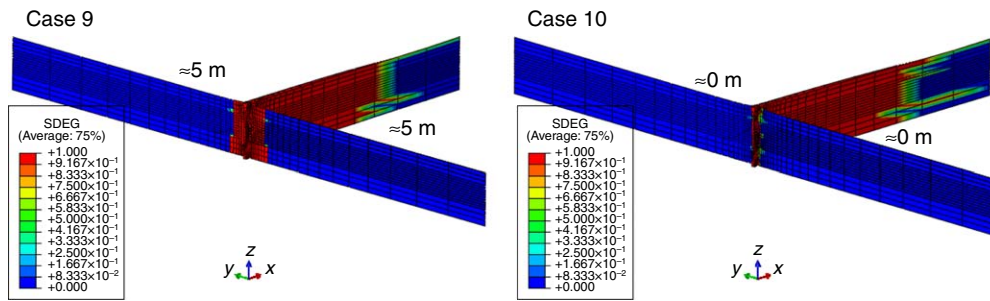


Fig. 43—SDEG plot for intersecting HF and NF planes at the end of pumping time for Case 9 (NF same as the surroundings) and Case 10 (NF stronger than the surroundings).

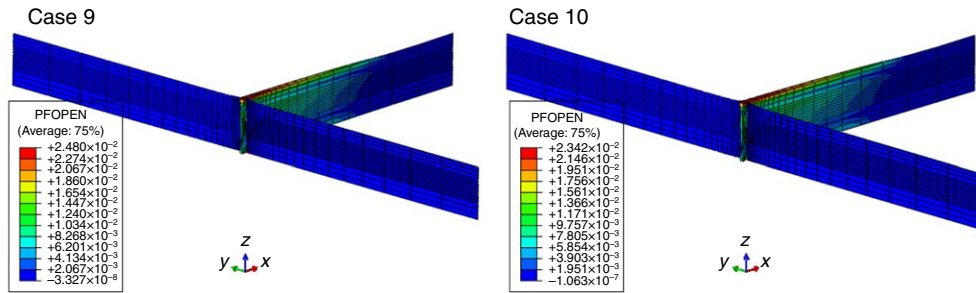


Fig. 44—Fracture opening for HF and NF planes at the end of pumping time for Case 9 (NF same as the surroundings) and Case 10 (NF stronger than the surroundings). PFOPEN = fracture opening output.

Case	Parameter	HF Observations	NF Observations
Base	$S_{Hmin} = 0.94 \cdot S_{Hmax}$, 30 bbl/min, 50 cp, weaker NF	Propagated through NF HF length in target zone ≈ 150 m	Target NF activated ≈ 150 m
1	$S_{Hmin} = 0.75 \cdot S_{Hmax}$	Propagated through NF Maximum HF opening with HF length and height in all the stress-contrast scenarios	Target NF activated ≈ 150 m Least in all stress-contrast scenarios
2	$S_{Hmin} = 0.99 \cdot S_{Hmax}$	Propagated through NF HF opening with HF length and height in almost the same as the base case	Target NF activated ≈ 150 m
3	Reversed S_{Hmin} and S_{Hmax}	Propagated along NF after intersection HF height contained in target zone HF opening less than the NF opening Totally different than the base case	NF activated completely NF opened up to ≈ 42 m in target zone
4	Injection rate = 15 bbl/min	Propagated through NF HF narrower and shorter as compared to the base case	Target NF activated ≈ 150 m
5	Injection rate = 60 bbl/min	Propagated through NF HF wider and longer as compared to the base case	Target NF activated ≈ 150 m
6	Injection-fluid viscosity = 10 cp	Propagated through NF HF narrower and longer as compared to the base case	Target NF activated ≈ 150 m
7	Injection-fluid viscosity = 1 cp	Propagated through NF HF narrowest and longest in all the viscosity effect scenarios	Target NF activated ≈ 180 m
8	Injection-fluid viscosity = 100 cp	Propagated through NF HF widest and shortest in all the viscosity effect scenarios	Target NF activated ≈ 105 m
9	NF the same as the surroundings	Propagated through NF HF length the same as the base case HF opening narrower than the base case	Target NF activated ≈ 5 m
10	Stronger NF	Propagated through NF HF length the same as the base case HF opening narrowest in all the NF-strength scenarios	Target NF activated ≈ 0 m

Table 3—Summarized results for different cases considered.

Notwithstanding the above, the simplifications we made in this work were not without their costs, especially as they related to the field applicability of our results. Validation on the basis of a field example with a calibrated NF model was not performed because of unavailability of data and the time constraint, but will be a part of future work. Also, as stated previously, we did not consider temperature-related stress effects caused by the injection of fracturing fluids and we did not include the effect of perforation pressure decline in our simulations. The intersection of the HF and NF at an angle other than 90° was also investigated without much success. We are continuing our investigation in this area and will attempt to remedy these drawbacks in future work.

Conclusions

The interaction of an orthogonally intersecting single HF and single NF was successfully modeled, for the first time, using the newly introduced advanced cohesive and pore-pressure elements FEA software capable of modeling the fluid continuity at the HF/NF intersection point.

In the case of an HF approaching an NF at a right angle, the HF crossed the NF (activating the NF but not opening the NF) for the scenarios considered, except for the stress-reversal scenario in which the HF was propagated into the NF instead of crossing it or propagating through it.

We observed, in the high-stress-contrast scenario, that the NF cohesive elements showed less damage when compared to the low-stress-contrast case. For a high-stress contrast with the principal horizontal stresses reversed, we observed that the HF was diverted into the NF. All the stress-contrast observations agreed with the laboratory findings in the literature. Keeping everything else constant, higher stress contrasts resulted in longer HFs and shorter activated NFs, while low or negligible stress contrast led to shorter HFs and longer activated NFs.

Increasing the injection rate resulted in longer and wider HFs without significant change in the NF-activated length. Hence, it was concluded that the injection rates in the range investigated (15 to 60 bbl/min) would lead to a similar NF-activated length but varying HF geometry for the model studied.

It was observed that injection-fluid viscosity had an inverse relationship with the HF length and a proportional relationship with the HF opening or width, as well as the NF-activated length.

A weak NF plane temporarily restricted the HF propagation. This was not seen in the case of stronger NF planes or NF planes having the same properties as the surrounding formation. Therefore, although the weaker NF temporarily restricted the HF propagation, it ultimately resulted in an HF with a wider opening and a longer NF-activated length.

Nomenclature

- c_b = bottom fluid leakoff coefficient, bbl/psia·min [M^2LT]
- c_t = top fluid leakoff coefficient, bbl/psia·min [M^2LT]
- d = cracked element opening, m [L]
- D = damage factor, dimensionless
- E = modulus of elasticity, kpsia [$ML^{-1}T^{-2}$]
- G = shear modulus, kpsia [$ML^{-1}T^{-2}$]
- G_{equiC} = equivalent fracture energy release rate, lbf/in. [MT^{-2}]
- G_{IC} = critical fracture energies in Mode-I, lbf/in. [MT^{-2}]
- G_{IIC} = critical fracture energies in Mode-II, lbf/in. [MT^{-2}]
- G_{II} and G_{III} = fracture energies utilized by the system during damage process, lbf/in. [MT^{-2}]
- k_t = tangential permeability, md [L^2]
- K = bulk modulus, kpsia [$ML^{-1}T^{-2}$]
- K_{IC} = fracture toughness, psia·in.^{1/2} [$ML^{-1/2}T^{-2}$]
- p = pore pressure, psia [$ML^{-1}T^{-2}$]
- p_0 = initial pore pressure, psia [$ML^{-1}T^{-2}$]
- p_b = pressure outside the bottom face of the fracture, psia [$ML^{-1}T^{-2}$]
- p_i = pressure inside the fracture, psia [$ML^{-1}T^{-2}$]
- p_t = pressure outside the top face of the fracture, psia [$ML^{-1}T^{-2}$]
- S_v = vertical stress, psia [$ML^{-1}T^{-2}$]
- S_{Hmax} = maximum horizontal stress, psia [$ML^{-1}T^{-2}$]
- S_{Hmin} = minimum horizontal stress, psia [$ML^{-1}T^{-2}$]
- t_n^o = damage initiation stress in the normal direction, kpsia [$ML^{-1}T^{-2}$]
- t_s^o = damage initiation stress in the shear direction, kpsia [$ML^{-1}T^{-2}$]
- t_t^o = damage initiation stress in the tangential direction, kpsia [$ML^{-1}T^{-2}$]
- t_n = stress in the element in the normal direction, kpsia [$ML^{-1}T^{-2}$]
- t_s = stress in the element in the shear direction, kpsia [$ML^{-1}T^{-2}$]
- t_t = stress in the element in tangential direction, kpsia [$ML^{-1}T^{-2}$]
- T_n = normal stress component, kpsia [$ML^{-1}T^{-2}$]
- T_s = shear stress component, kpsia [$ML^{-1}T^{-2}$]
- T_t = tangential stress component, kpsia [$ML^{-1}T^{-2}$]
- v_b = flow velocity into the bottom surface of the cracked element, m/s [LT^{-1}]
- v_t = flow velocity into the top surface of the cracked element, m/s [LT^{-1}]
- α = Biot's constant, dimensionless
- δ_{ij} = Kronecker's delta
- $\frac{\partial d}{\partial t}$ = change in the fracture opening per change in time, in./sec [LT^{-1}]
- $\frac{\partial q}{\partial l}$ = change in the fracture fluid rate per change in fracture length, bbl/min·m [$M^3L^{-1}T^{-1}$]

ε'_{ij} = Terzaghi's effective strain, dimensionless
 η = material parameter, dimensionless
 μ = viscosity of the injection fluid, cp [$\text{ML}^{-1}\text{T}^{-1}$]
 ϑ = Poisson's ratio, dimensionless
 σ'_{ij} = Terzaghi's effective stress, psia [$\text{ML}^{-1}\text{T}^{-2}$]
 ∇p = pressure gradient along the cracked element surfaces, psia/m [$\text{ML}^{-2}\text{T}^{-2}$]

References

- Abbas, S., Gordeliy, E., Peirce, A. et al. 2014. Limited Height Growth and Reduced Opening of Hydraulic Fractures Due to Fracture Offsets: An XFEM Application. Presented at the SPE Hydraulic Fracturing Technology Conference, The Woodlands, Texas, 4–6 February. SPE-168622-MS. <https://doi.org/10.2118/168622-MS>.
- Aimene, Y. E. and Nairn, J. A. 2014. Modeling Multiple Hydraulic Fractures Interacting with Natural Fractures Using the Material Point Method. Presented at the SPE/EAGE European Unconventional Resources Conference and Exhibition, Vienna, Austria, 25–27 February. SPE-167801-MS. <https://doi.org/10.2118/167801-MS>.
- Barree, R. D. and Mukherjee, H. 1996. Determination of Pressure Dependent Leakoff and Its Effect on Fracture Geometry. Presented at the SPE Annual Technical Conference and Exhibition, Denver, 6–9 October. SPE-36424-MS. <https://doi.org/10.2118/36424-MS>.
- Ben, Y., Miao, Q., Wang, Y. et al. 2012. Effect of Natural Fractures on Hydraulic Fracturing. Presented at the ISRM Regional Symposium–7th Asian Rock Mechanics Symposium, Seoul, Korea, 15–19 October. ISRM-ARMS7-2012-087.
- Benzeggah, M. L. and Kennane, M. 1996. Measurement of Mixed-Mode Delamination Fracture Toughness of Unidirectional Glass/Epoxy Composites with Mixed-Mode Bending Apparatus. *Compos Sci Technol* **56**: 439–449. [https://doi.org/10.1016/0266-3538\(96\)00005-X](https://doi.org/10.1016/0266-3538(96)00005-X).
- Blanton, T. L. 1982. An Experimental Study of Interaction Between Hydraulically Induced and Pre-Existing Fractures. Presented at the SPE Unconventional Gas Recovery Symposium, Pittsburgh, Pennsylvania, 16–18 May. SPE-10847-MS. <https://doi.org/10.2118/10847-MS>.
- Charlez, P. A. 1997. The Impact of Constitutive Laws on Wellbore Stability: A General Review. *SPE J.* **12** (2): 119–128. SPE-28058-PA. <https://doi.org/10.2118/28058-PA>.
- Chuprakov, D. A., Akulich, A. V., Siebrits, E. et al. 2011. Hydraulic-Fracture Propagation in a Naturally Fractured Reservoir. *SPE Prod & Oper* **26** (1): 88–97. SPE-128715-PA. <https://doi.org/10.2118/128715-PA>.
- Chuprakov, D., Melchaeva, O., and Prioul, R. 2013. Hydraulic Fracture Propagation Across a Weak Discontinuity Controlled by Fluid Injection. Presented at the ISRM International Conference for Effective and Sustainable Hydraulic Fracturing, Brisbane, Australia, 20–22 May. ISRM-ICHF-2013-008.
- COMSOL Multiphysics is a registered trademark of Comsol AB, Tegnergatan 23 SE-111 40, Stockholm, Sweden. <https://www.comsol.com/release/5.4>.
- Dahi Taleghani, A.. 2009. *Analysis of Hydraulic Fracture Propagation in Fractured Reservoirs: An Improved Model for Interaction Between Induced and Natural Fractures*. PhD dissertation, University of Texas, Austin, Texas (May 2009).
- Dahi Taleghani, A. and Olson, J. E. 2014. How Natural Fractures Could Affect Hydraulic-Fracture Geometry. *SPE J.* **19** (1): 161–171. SPE-167608-PA. <https://doi.org/10.2118/167608-PA>.
- Fisher, M. K., Wright, C. A., Davidson, B. M. et al. 2002. Integrating Fracture Mapping Technologies To Optimize Stimulations in the Barnett Shale. Presented at the SPE Annual Technical Conference and Exhibition, San Antonio, Texas, 29 September–2 October 2002. SPE-77441-MS. <https://doi.org/10.2118/77441-MS>.
- FLAC is a registered trademark of Itasca Consulting Group, Inc., 111 Third Avenue South, Suite 450, Minneapolis, Minnesota 55401. <https://www.itascacsg.com/software/flac>.
- Fu, P., Cruz, L., Moos, D. et al. 2015. Numerical Investigation of a Hydraulic Fracture Bypassing a Natural Fracture in 3D. Presented at the 49th U.S. Rock Mechanics/Geotechnics Symposium, San Francisco, 28 June–1 July. ARMA-2015-671.
- Fu, P., Johnson, S. M., and Carrigan, C. R. 2011. Simulating Complex Fracture Systems in Geothermal Reservoirs Using an Explicitly Coupled Hydro-Geomechanical Model. Presented at the 45th U.S. Rock Mechanics/Geomechanics Symposium, San Francisco, 26–29 June. ARMA-11-244.
- GEOS is a trademark of Lawrence Livermore National Laboratory, 7000 East Avenue, Livermore, California 94550-9234. <https://str.llnl.gov/july-2014/ryerson>.
- Gong, B., Qin, G., Towler, B. F. et al. 2011. Discrete Modeling of Natural and Hydraulic Fractures in Shale-Gas Reservoirs. Presented at the SPE Annual Technical Conference and Exhibition, Denver, 30 October–2 November. SPE-146842-MS. <https://doi.org/10.2118/146842-MS>.
- Gonzalez-Chavez, M., Puyang, P., and Dahi Taleghani, A. 2015. From Semi-Circular Bending Test to Micro Seismic Maps: An Integrated Modeling Approach To Incorporate Natural Fracture Effects on Hydraulic Fracturing. Presented at the Unconventional Resources Technology Conference, San Antonio, Texas, 20–22 July. SPE-178544-MS. <https://doi.org/10.2118/178544-MS>.
- Gu, H., Weng, X., Lund, J. B. et al. 2011. Hydraulic Fracture Crossing Natural Fracture at Non-Orthogonal Angles, a Criterion, Its Validation and Applications. Presented at the SPE Hydraulic Fracturing Technology Conference, The Woodlands, Texas, 24–26 January. SPE-139984-MS. <https://doi.org/10.2118/139984-MS>.
- Haddad, M. and Sepehrmoori, K. 2014. Simulation of Multiple-Stage Fracturing in Quasibrittle Shale Formations Using Pore Pressure Cohesive Zone Model. Presented at the Unconventional Resources Technology Conference, Denver, 25–27 August. URTEC-1922219-MS. <https://doi.org/10.15530/URTEC-2014-1922219>.
- Haddad, M. and Sepehrmoori, K. 2015. XFEM-Based CZM for the Simulation of 3D Multiple-Stage Hydraulic Fracturing in Quasi-Brittle Shale Formations. Presented at the AADE National Technical Conference and Exhibition, San Antonio, Texas, 8–9 April 2015. AADE-15-NTCE-28.
- He, M. Y. and Hutchinson, J. W. 1989. Crack Deflection at an Interface Between Dissimilar Elastic Materials. *Int J Solids Struct* **25** (9): 1053–1067. [https://doi.org/10.1016/0020-7683\(89\)90021-8](https://doi.org/10.1016/0020-7683(89)90021-8).
- Jeffrey, R. G., Zhang, X., and Thiercelin, M. J. 2009. Hydraulic Fracture Offsetting in Naturally Fractured Reservoirs: Quantifying a Long-Recognized Process. Presented at the SPE Hydraulic Fracturing Technology Conference, The Woodlands, Texas, 19–21 January. SPE-119351-MS. <https://doi.org/10.2118/119351-MS>.
- Koshelev, V. and Ghassemi, A. 2003. Numerical Modeling of Stress Distribution and Crack Trajectory Near a Fault or a Natural Fracture. *Proc., Soil and Rock America*, Cambridge, Massachusetts, 22–26 June, H0129C, 931–935.
- Kresse, O. and Weng, X. 2013. Hydraulic Fracturing in Formations with Permeable Natural Fractures. Presented at the ISRM International Conference for Effective and Sustainable Hydraulic Fracturing, Brisbane, Australia, 20–22 May. ISRM-ICHF-2013-028.
- Lancaster, D. E., McKetta, S. F., Hill, R. E. et al. 1992. Reservoir Evaluation, Completion Techniques, and Recent Results from Barnett Shale Development in the Fort Worth Basin. Presented at the Offshore Technology Conference–Asia, Kuala Lumpur, 25–28 March. SPE-24884-MS. <https://doi.org/10.2118/24884-MS>.

- Lecampion, B. 2009. An Extended Finite Element for Hydraulic Fracture Problems. *Int J Numer Method Biomed Eng* **25** (2): 212–133. <https://doi.org/10.1002/cnm.1111>.
- Lu, C., Li, M., Guo, J.-C. et al. 2015. Engineering Geological Characteristics and the Hydraulic Fracture Propagation Mechanism of the Sand-Shale Interbedded Formation in the Xu5 Reservoir. *J Geophys Eng* **12** (3): 321–339. <https://doi.org/10.1088/1742-2132/12/3/321>.
- Meng, C. and De Pater, H. J. 2011. Hydraulic Fracture Propagation in Pre-Fractured Natural Rocks. Presented at the SPE Hydraulic Fracturing Technology Conference, The Woodlands, Texas, 24–26 January. SPE-140429-MS. <https://doi.org/10.2118/140429-MS>.
- Moës, N., Dolbow, J., and Belytschko, T. 1999. A Finite Element Method for Crack Growth without Remeshing. *Int J Numer Method Biomed Eng* **46** (1): 131–150. [https://doi.org/10.1002/\(SICI\)1097-0207\(19990910\)46:1<131::AID-NME726>3.0.CO;2-J](https://doi.org/10.1002/(SICI)1097-0207(19990910)46:1<131::AID-NME726>3.0.CO;2-J).
- Mukherjee, H., Larkin, S., and Kordziel, W. 1991. Extension of Fracture Pressure Decline Curve Analysis to Fissured Formations. Presented at the Low Permeability Reservoirs Symposium, Denver, 15–17 April. SPE-21872-MS. <https://doi.org/10.2118/21872-MS>.
- Nagel, N. B., Gil, I., Sanchez-Nagel, M. et al. 2011. Simulating Hydraulic Fracturing in Real Fractured Rocks—Overcoming the Limits of Pseudo3D Models. Presented at SPE Hydraulic Fracturing Technology Conference, The Woodlands, Texas, 24–26 January. SPE-140480-MS. <https://doi.org/10.2118/140480-MS>.
- Nagel, N. B., Sanchez-Nagel, M., Lee, B. et al. 2012. Hydraulic Fracturing Optimization for Unconventional Reservoirs—The Critical Role of the Mechanical Properties of the Natural Fracture Network. Presented at SPE Canadian Unconventional Resources Conference, Calgary, 30 October–1 November. SPE-161934-MS. <https://doi.org/10.2118/161934-MS>.
- Nolte, K. G. 1991. Fracturing-Pressure Analysis for Nonideal Behavior. *J Pet Technol* **43** (2): 210–218. SPE-20704-PA. <https://doi.org/10.2118/20704-PA>.
- Nolte, K. G. and Smith, M. B. 1981. Interpretation of Fracturing Pressures. *J Pet Technol* **33** (9): 1767–1775. SPE-8297-PA. <https://doi.org/10.2118/8297-PA>.
- Offenberger, R., Ball, N., Kanneganti, K. et al. 2013. Integration of Natural and Hydraulic Fracture Network Modeling with Reservoir Simulation for an Eagle Ford Well. Presented at the SPE/AAPG/SEG Unconventional Resources Technology Conference, Denver, 12–14 August. URTEC-1563066-MS. <https://doi.org/10.1190/URTEC2013-049>.
- Olson, J. E. and Pollard, D. D. 1991. The Initiation and Growth of En Echelon Vents. *J Struct Geol* **13** (5): 595–608. [https://doi.org/10.1016/0191-8141\(91\)90046-L](https://doi.org/10.1016/0191-8141(91)90046-L).
- Oussoltsev, D., Offenberger, R. M., Kanneganti, K. T. et al. 2013. Application of Reservoir-Centric Stimulation Design Tool in Completion Optimization for Eagle Ford Shale. Presented at the SPE Unconventional Resources Conference-USA, The Woodlands, Texas, 10–12 April. SPE-164526-MS. <https://doi.org/10.2118/164526-MS>.
- Searles, K. H., Zielonka, M. G., Ning, J. et al. 2016. Fully Coupled 3D Hydraulic Fracture Models: Development, Validation, and Application to O&G Problems. Presented at the SPE Hydraulic Fracturing Technology Conference, The Woodlands, Texas, 9–11 February. SPE-179121-MS. <https://doi.org/10.2118/179121-MS>.
- Sesetty, V. and Ghassemi, A. 2012. Simulation of Hydraulic Fractures and Their Interactions with Natural Fractures. Presented at the 46th U.S. Rock Mechanics/Geomechanics Symposium, Chicago, Illinois, 24–27 June. ARMA-2012-331.
- Shin, D. H. and Sharma, M. M. 2014. Factors Controlling the Simultaneous Propagation of Multiple Competing Fractures in a Horizontal Well. Presented at the SPE Hydraulic Fracturing Technology Conference, The Woodlands, Texas, 4–6 February. SPE-168599-MS. <https://doi.org/10.2118/168599-MS>.
- Suarez-Rivera, R., Burghardt, J., Edelman, E. et al. 2013. Geomechanics Considerations for Hydraulic Fracture Productivity. Presented at the 47th U.S. Rock Mechanics/Geomechanics Symposium, San Francisco, 23–26 June. ARMA-2013-666.
- Unconventional Fracture Model (UFM) is a service mark of Schlumberger Limited, 300 Schlumberger Dr., Sugar Land, Texas 77478. <https://www.software.slb.com/products/kinetix/kinetix-shale>.
- Walsh, J. B. 1981. Effect of Pore Pressure and Confining Pressure on Fracture Permeability. *Int J Rock Mech Min Sci Geomech Abstr* **18** (5): 429–435. [https://doi.org/10.1016/0148-9062\(81\)90006-1](https://doi.org/10.1016/0148-9062(81)90006-1).
- Warpinski, N. R. 1991. Hydraulic Fracturing in Tight, Fissured Media. *J Pet Technol* **43** (2): 146–209. SPE-20154-PA. <https://doi.org/10.2118/20154-PA>.
- Warpinski, N. R. and Teufel, L. W. 1987. Influence of Geologic Discontinuities on Hydraulic Fracture Propagation. *J Pet Technol* **39** (2): 209–220. SPE-13224-PA. <https://doi.org/10.2118/13224-PA>.
- Weng, X., Kresse, O., Cohen, C.-E. et al. 2011. Modeling of Hydraulic-Fracture-Network Propagation in a Naturally Fractured Formation. *SPE Prod & Oper* **26** (1): 368–380. SPE-140253-PA. <https://doi.org/10.2118/140253-PA>.
- Yadav, H. 2011. *Hydraulic Fracturing in Naturally Fractured Reservoirs and the Impact of Geomechanics on Micro Seismicity*. MS thesis, University of Texas, Austin, Texas (December 2011).
- Zhang, X. and Jeffrey, R. G. 2006. The Role of Friction and Secondary Flaws on Deflection and Re-Initiation of Hydraulic Fractures at Orthogonal Pre-Existing Fractures. *Geophys J Int* **166** (3): 1454–1465. <https://doi.org/10.1111/j.1365-246X.2006.03062.x>.
- Zielonka, M. G., Searles, K. H., Ning, J. et al. 2014. Development and Validation of Fully Coupled Hydraulic Fracturing Simulation Capabilities. Presented at the SIMULIA Community Conference, Providence, Rhode Island, 20 May.

Aditya Nikam is a drilling and completions optimization engineer at Etech International Inc. His interests include rock mechanics and fracture modeling. Nikam's recent publications include studies on the geomechanical interaction between hydraulic and natural fractures to lay down design roadmaps for better fracture treatments. He holds a BS degree from Pune University in India and an MS degree from the University of Alaska, Fairbanks, both in petroleum engineering. Nikam is a member of SPE.

Obadare O. Awoleke is an assistant professor at the University of Alaska, Fairbanks. His research interests include production engineering, experimental investigations into petroleum engineering phenomena, the incorporation of uncertainty into petroleum engineering models, and data mining/analytics. Awoleke holds a BS degree from the University of Ibadan, Nigeria, and MS and PhD degrees from Texas A&M University, all in petroleum engineering. He is a member of SPE.

Mohabbat Ahmadi is an associate professor at the University of Alaska, Fairbanks. His research interests include oil and gas phase behavior, reservoir-rock wettability alteration, high-pressure/high-temperature coreflooding experiments for gas/condensate flow in porous media, theoretical work related to production-decline data analysis, conventional and unconventional-reservoir simulation, CO₂ EOR, and sequestration and methane extraction from coalbeds. Ahmadi has authored or coauthored more than 20 technical papers and has reviewed more than 20 papers for various journals. He holds BS and MS degrees from the Petroleum University of Technology, Ahwaz, Iran, and a PhD degree from the University of Texas at Austin, all in petroleum engineering. Ahmadi is a recipient of the 2017 SPE Regional Distinguished Achievement Award for Petroleum Engineering Faculty for the Western North American Region and is a member of SPE.